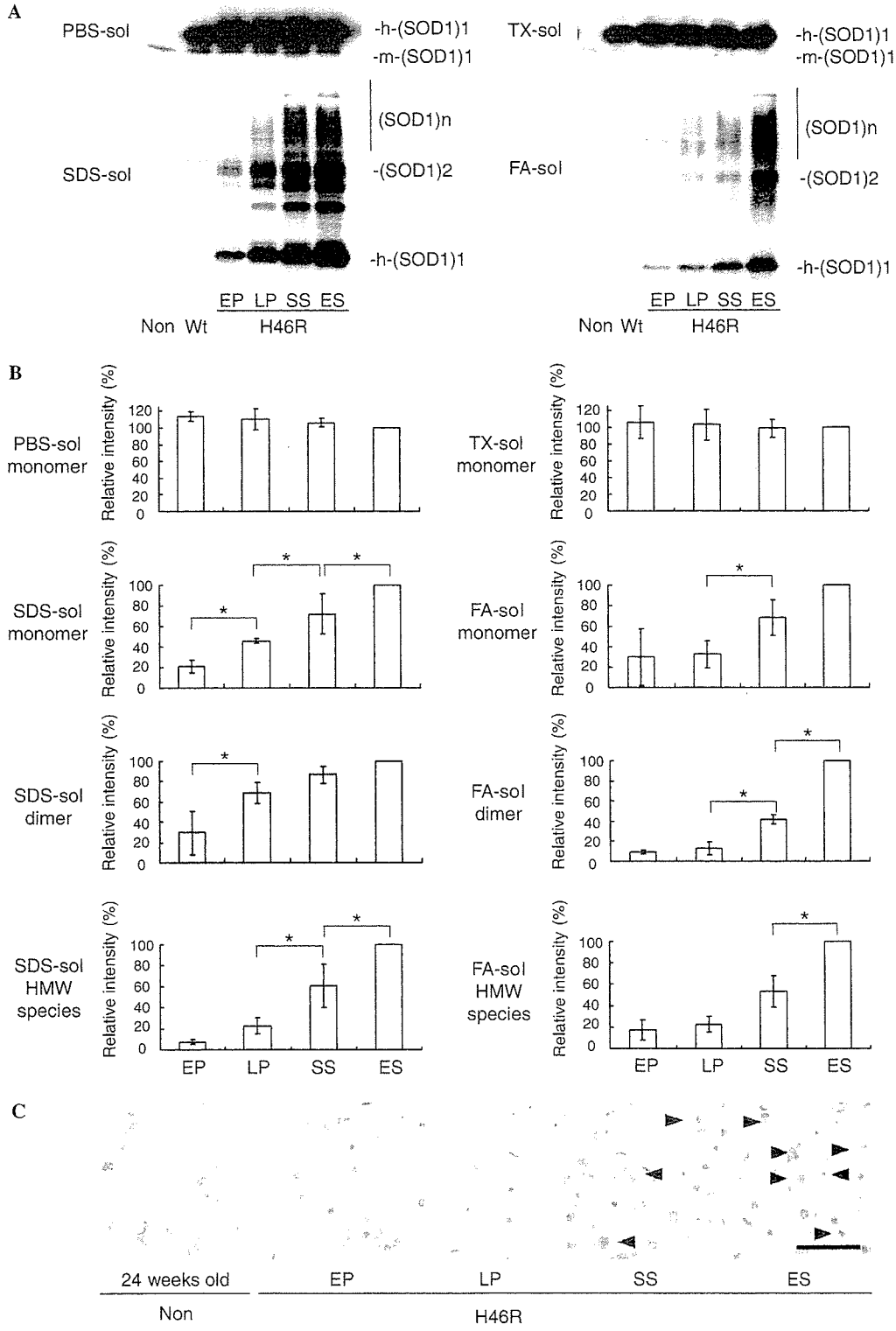

Fig. 2. Age-dependent alteration of SOD1 in spinal cords from H46R SOD1 transgenic mice. (A) The spinal cords of 24-week-old non-transgenic littermates (Non), 38-week-old wild-type SOD1 transgenic mice (Wt), and H46R SOD1 transgenic mice (H46R) at early presymptomatic stage (EP), late presymptomatic stage (LP), symptomatic stage (SS), and end stage (ES) were sequentially fractionated. Ten micrograms of protein from each of the PBS-soluble fraction (PBS-sol), the TX-soluble fraction (TX-sol), and the SDS-soluble fraction (SDS-sol), and equal aliquots of the FA-soluble fraction (FA-sol) were loaded on the gel and then immunoblotted with SOD1-100 antibody. (B) The graphs represent relative intensities of H46R SOD1 species at each stage ($n = 3$, bars represent mean ± SD, $^{*}P < 0.05$). (C) Immunohistochemical analysis of lumbar spinal cords (L_{4-5}) of 24-week-old non-transgenic littermates (Non) and H46R SOD1 transgenic mice (H46R) at four stages. These sections were immunostained with monoclonal anti-SOD1 antibody specific to human SOD1. Scale bars = 50 μm. Arrowheads indicate SOD1-immunoreactive structures.

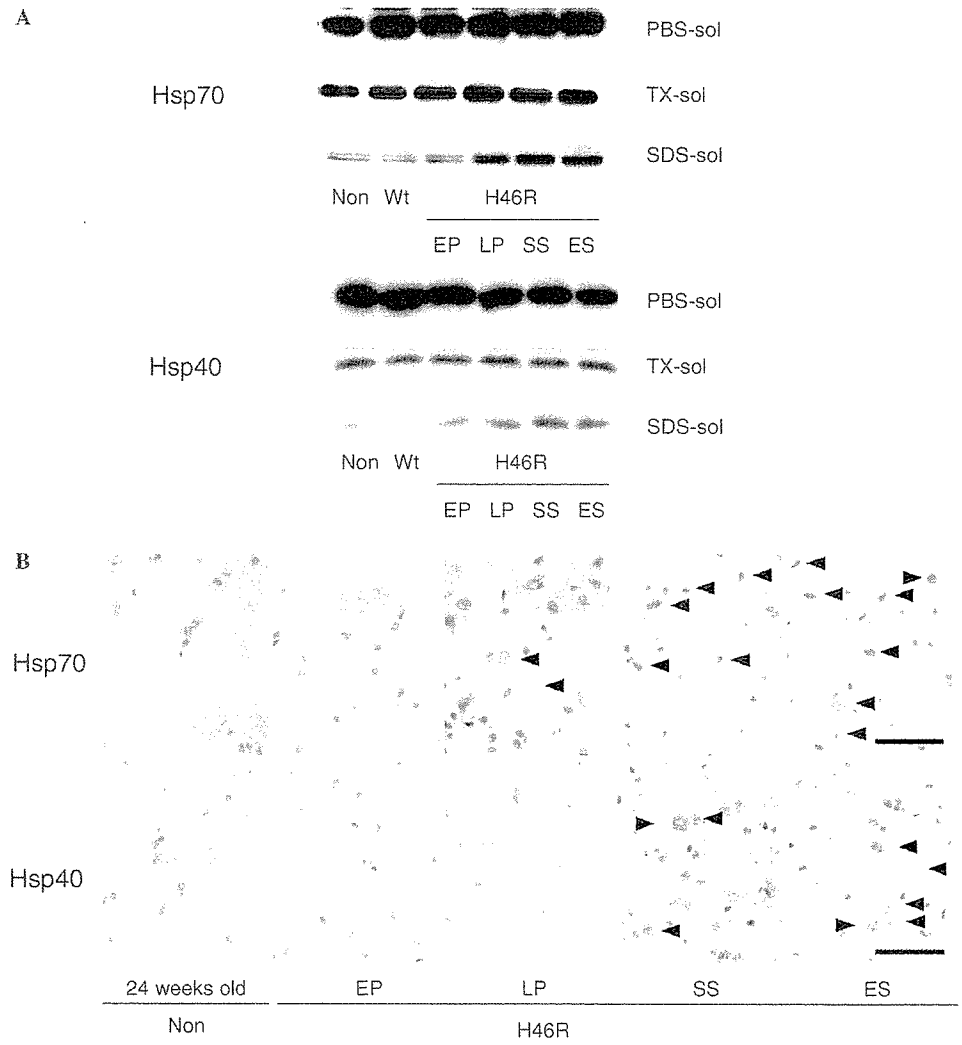

Fig. 3. (A) Increase of Hsp70 and Hsp40 in the SDS-soluble fraction from H46R SOD1 transgenic mice. The fractionated samples used in Fig. 2 were analyzed by Western blotting using anti-Hsp70 and anti-Hsp40 antibodies. Ten micrograms of total protein from each fraction was loaded on each lane. (B) Time course analysis of Hsp-immunoreactive structures. These sections were immunostained with anti-Hsp70 antibody and anti-Hsp40 antibody. Scale bars = 50 μm. Arrowheads indicate immunoreactive structures of each antibody.

the serial sections (data not shown). Although a small number of Hsp70-positive structures were found in neuropil at LP, the increase of SOD1-inclusions containing Hsp70 immunoreactivities was remarkable after SS (Fig. 3B). Similarly, Hsp40-positive structures increased from SS (Fig. 3B). The present data showed that the increase of Hsp70 and Hsp40 in the SDS-soluble fraction appeared along with the increase of SDS-dissociable soluble SOD1 monomers and SDS-stable soluble dimers. This increase of Hsp70 and Hsp40 occurred before the accumulation of visible inclusions with Hsp70 and Hsp40 immunoreactivities.

Inhibition of the proteasome activity promotes the change of SOD1 solubility in cells expressing H46R SOD1

The fALS-linked mutant misfolded SOD1 protein is reported to be degraded by the proteasome pathway [16,17,19,20]. To see how inhibition of the proteasome pathway influences mutant SOD1 solubility, we examined COS-7 cells transiently overexpressing either wild-type SOD1-FLAG or H46R SOD1-FLAG in the presence or absence of proteasome inhibitor MG132. In this experiment, FLAG-tagged SOD1 was used for discriminating exogenous SOD1 from endogenous SOD1 by migrating more slowly. Collected cell pellets were sequentially extracted with PBS, 1% TX, and 5% SDS. In the PBS-soluble and the TX-soluble fractions, the levels of mutant SOD1 as well as wild-type SOD1 slightly increased when MG132 was added in a dose-dependent manner (Fig. 4A). In the SDS-soluble fraction, a small amount of wild-type monomeric SOD1 was seen in the absence of MG132. The levels of wild-type SOD1 monomers increased without generating HMW species in the presence of 10 μM MG132. On the other hand, in the SDS-soluble fraction, mutant SOD1 monomers and dimers were obviously

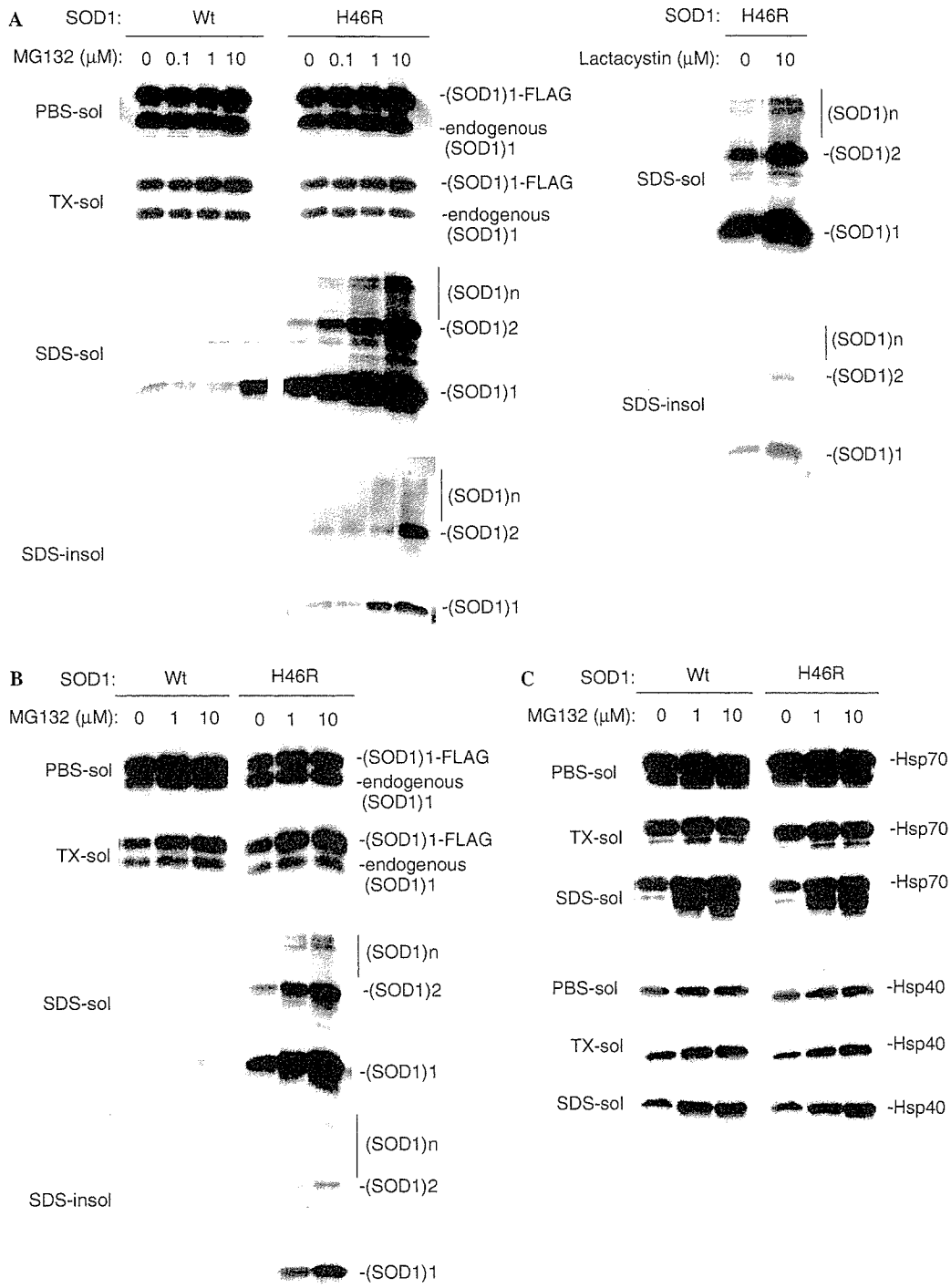

Fig. 4. Alteration of H46R SOD1 solubility in COS-7 and SH-SY5Y cells by treatment with proteasome inhibitors. COS-7 cells (A) and SH-SY5Y cells (B,C) were transiently transfected with either wild-type SOD1-FLAG pcDNA3.1 or H46R SOD1-FLAG pcDNA3.1. At 24 h after transfection, the culture medium was replaced with a fresh one containing the indicated concentrations of proteasome inhibitor, either MG132 (left panels of (A) and all panels of (B)) or lactacystin (right panels of (A)). Cells were incubated for an additional 24 h. Collected cell pellets were serially fractionated to the PBS-soluble fraction (PBS-sol), the TX-soluble fraction (TX-sol), the SDS-soluble fraction (SDS-sol), and the SDS-insoluble fraction (SDS-insol). Ten micrograms of protein from each of the PBS-soluble fraction, the TX-soluble fraction, and the SDS-soluble fraction, and equal aliquots of the SDS-insoluble fraction were subjected to the gel and immunoblotted with SOD1-100 (A,B). (C) The levels of both endogenous Hsp70 and Hsp40 were elevated in the SDS-soluble fraction from cells expressing wild-type SOD1 as well as mutant SOD1 in an MG-132 dose-dependent manner. The fractionated samples used in (B) were analyzed by Western blotting using anti-Hsp70 and anti-Hsp40 antibodies.

detected in the absence of MG132 and showed a significant increase in generating HMW species by treatment with MG132 in a dose-dependent manner (Fig. 4A). Similarly, in the SDS-insoluble fraction, the levels of mutant SOD1 monomers, dimers, and HMW species elevated by treatment with MG132 in a dose-dependent manner, while wild-type SOD1 was not detected (Fig. 4A). Dose-dependent treatment with MG132 further showed that the elevation of SDS-dissociable soluble mutant SOD1 monomers and SDS-stable soluble dimers preceded that of SDS-stable soluble HMW species and SDS-insoluble species. Treatment with another specific proteasome inhibitor, lactacystin, also caused the accumulation of SDS-soluble and SDS-insoluble mutant SOD1 species in COS-7 cells, although to a lesser extent (Fig. 4A). We further confirmed the effect of MG132 on the alteration of SOD1 solubility in human neuroblastoma SH-SY5Y cells. By treatment with MG132, SDS-soluble and SDS-insoluble mutant SOD1 monomers, dimers, and HMW species accumulated in mutant-specific and dose-dependent manners in SH-SY5Y cells similar to COS-7 cells (Fig. 4B). The elevation of SDS-dissociable soluble mutant SOD1 monomers and SDS-stable soluble dimers also preceded that of SDS-stable soluble HMW species and SDS-insoluble species. In SH-SY5Y cells expressing mutant SOD1, the levels of both endogenous Hsp70 and Hsp40 were elevated in the SDS-soluble fraction in an MG-132 dose-dependent manner (Fig. 4C). However, the increase of endogenous Hsp70 and Hsp40 levels in the SDS-soluble fraction was similarly observed in cells expressing wild-type SOD1 (Fig. 4C). These results showed that inhibition of the proteasome activity in mutant SOD1 expressed cells recapitulated the alteration of SOD1 solubility with aging in mutant transgenic mice. Inhibition of the proteasome activity initially led to the accumulation of SDS-dissociable soluble mutant SOD1 monomers and SDS-stable soluble dimers prior to that of SDS-stable soluble HMW species and SDS-insoluble species irrespective of the increase of endogenous Hsp70 and Hsp40.

Effect of overexpression of Hsp70 on the accumulation of SDS-soluble and SDS-insoluble mutant SOD1 species

Overexpression of Hsp70 has been reported to reduce the SOD1-aggregate formation and prolong cellular viability in a cellular model of fALS [23]. As described in our previous report [20], overexpression of mutant SOD1 pEF-BOS in COS-7 cells causes higher expression levels of SOD1 than overexpression of mutant SOD1 pcDNA3.1, and a large amount of SDS-insoluble mutant SOD1 appears without adding proteasome inhibitor. By taking advantage of this high-expression system, we investigated cells co-transfected with mutant H46R SOD1 cDNA and a 4-fold molar excess of Hsp cDNA to see the effect of Hsp70 and Hsp40 on the levels of altered insoluble SOD1 species (Fig. 5A). Overexpression of Hsp70 obviously reduced the levels of SDS-dissociable soluble mutant SOD1 monomers, SDS-stable soluble dimers, and SDS-stable soluble HMW species, compared to co-expression of the empty vector (Fig. 5A). Overexpression of Hsp40 showed a weaker effect on the levels of SDS-soluble mutant SOD1 species (Fig. 5A). Co-overexpression with Hsp70 plus Hsp40 enhanced the effect of Hsp70 on a decrease of the levels of SDS-stable soluble mutant SOD1 dimers and HMW species (Fig. 5A). In the SDS-insoluble fraction, overexpression of Hsp70 also led to a reduction in the levels of SDS-dissociable insoluble mutant SOD1 monomers, SDS-stable insoluble dimers, and SDS-stable insoluble HMW species, and the effect was enhanced by co-overexpression of Hsp40 (Fig. 5A). This finding was also observed in cells expressing different fALS-linked mutant G93A SOD1 (data not shown). To further examine the molecular mechanism by which overexpression of Hsp70 reduced insoluble mutant SOD1 species, cells were co-transfected with H46R SOD1 and Hsp70 cDNAs in various molar ratios (Fig. 5B). The levels of mutant SOD1 monomers, dimers, and HMW species in the SDS-soluble fraction as well as in the SDS-insoluble fraction decreased in negative correlation to the amounts of transfected Hsp70 cDNA (Figs. 5B and C). On the other hand, the levels of mutant SOD1 monomers in the PBS-soluble and TX-soluble fractions did not increase, in sharp contrast to the significant reduction of the amount of SDS-soluble species by overexpression of Hsp70 (Figs. 5B and C). These findings demonstrated that overexpressed Hsp70 modulated the levels at SDS-dissociable soluble mutant SOD1 monomers and SDS-stable soluble dimers as misfolded proteins and preferentially forwarded abnormally insoluble SOD1 species to degradation rather than to refolding.

Discussion

Although wild-type SOD1 is principally a soluble, cytosolic protein [4], fALS-linked mutant SOD1 has a tendency to assemble as insoluble aggregates, which are immunohistochemically observed as cytoplasmic inclusions in patients with fALS having SOD1 mutation [10]. There has been controversy about whether such inclusions are a cause or simply a result of the neuronal degeneration. Immunohistochemical experiments do not rule out the possibility that mutant SOD1 aggregates can damage motor neurons, even though microscopically visible inclusions are absent in the early period. In agreement with the previous finding [16,19], our immunohistochemical data demonstrated that SOD1-positive inclusions appeared after disease onset, and the accumulation of SOD1-positive inclusions was parallel to the elevation of most insoluble SOD1 species recovered in the FA-soluble fraction. On the other hand, we revealed that mutant H46R SOD1 began to significantly alter its solubility to SDS-dissociable soluble monomers and SDS-stable soluble dimers earlier than the appearance of visible SOD1-positive inclusions. These findings suggest that complexes of SDS-dissociable soluble SOD1 monomers and SDS-stable soluble dimers were much smaller in

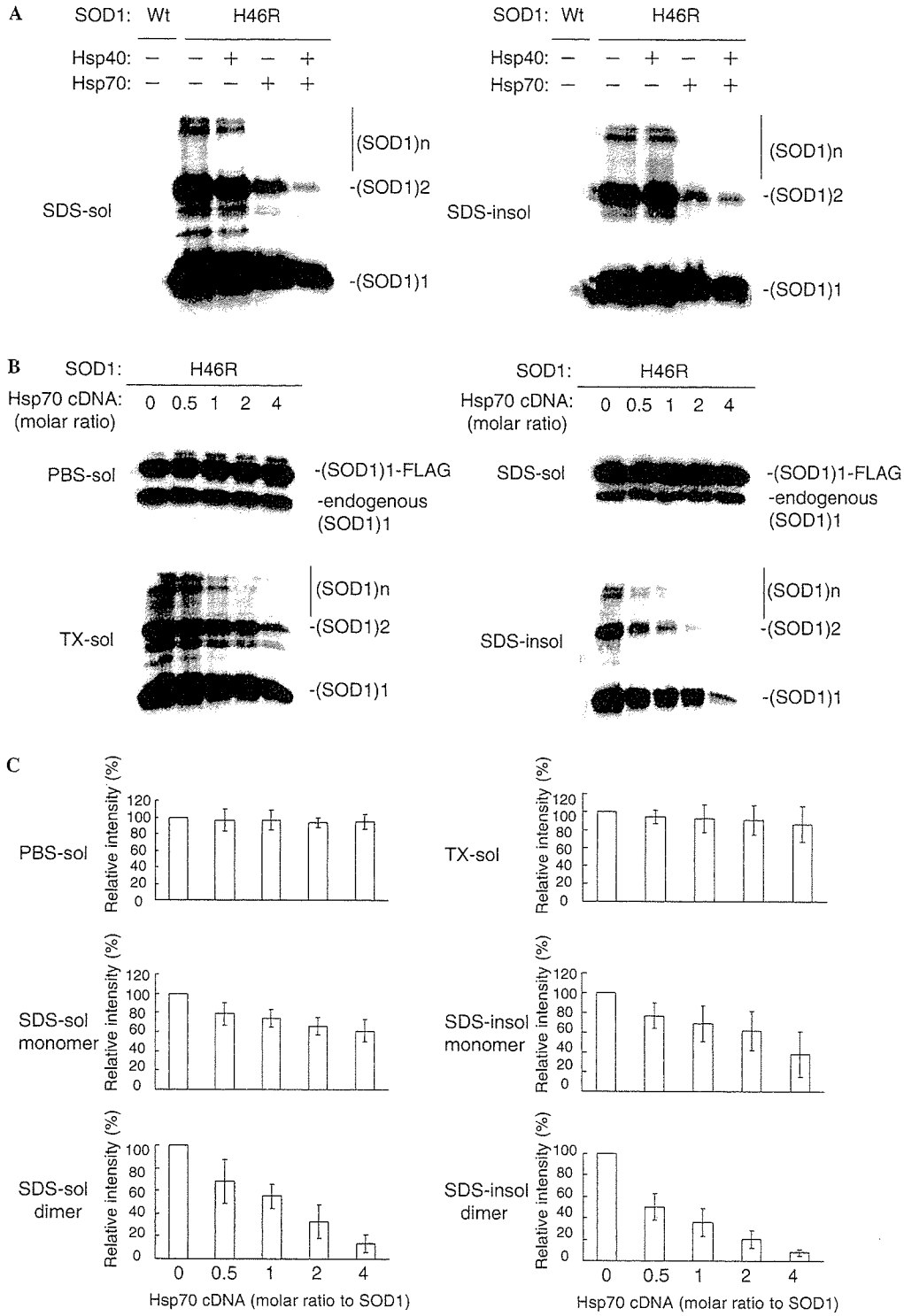

Fig. 5. The effect of overexpression of Hsp70 and Hsp40 on the level of altered insoluble mutant SOD1 in intact cells. (A) Western blots of COS-7 cells co-transfected with H46R SOD1-FLAG pEF-BOS and either pCMV-Hsp70 or pRC-Hsp40 (molar ratio of Hsp versus SOD1 cDNA was 4:1) using SOD1-100 antibody. Proteins from the SDS-soluble (SDS-sol) and SDS-insoluble (SDS-insol) fractions were loaded to the gel and immunoblotted with SOD1-100 antibody. (B) Western blot analysis of cells co-transfected with H46R SOD1-FLAG pEF-BOS and various amounts of Hsp70 cDNA. Molar ratios of pCMV-Hsp70 versus H46R SOD1-FLAG pEF-BOS are indicated in the figure. Forty-eight hours after transfection, cells were harvested and fractionated. Proteins from each fraction were analyzed by Western blotting using an SOD1-100 antibody. (C) The graphs show the relative intensities of H46R SOD1 monomers and dimers in each fraction shown in (B). The relative intensities were quantified by densitometry and normalized to bands from cells transfected with the empty vector ($n = 3$, bars represent mean ± SD).

size than visible inclusions, and the presence of visible inclusions composed of highly insoluble aggregates contributes less to the early pathological event.

Our findings are relevant to the previous reports that detergent-insoluble dimers and HMW species were found before onset of motor disability and the appearance of pathological SOD1-aggregates in mutant SOD1 transgenic mice [16,19]. However, in these preceding experiments, the alteration of mutant SOD1 solubility was assessed by fractionation using only one detergent. By the sequential extraction of mutant transgenic mouse spinal cords with PBS and TX containing buffer for removing cytosolic and mitochondrial SOD1 with normal solubility equivalent to wild-type SOD1, we separated H46R SOD1 into three different kinds of mutant-specific insoluble species, indicating that insoluble mutant SOD1 did not consist of a uniform species. To see whether SDS-dissociable soluble monomers, in addition to SDS-stable soluble dimers, represented early misfolded intermediates, we have investigated the alteration of SOD1 solubility using a cell culture model of fALS. Treatment with proteasome inhibitors caused the accumulation of SDS-dissociable soluble mutant H46R SOD1 monomers and SDS-stable soluble dimers earlier than that of SDS-stable soluble HMW species and SDS-insoluble species. This finding resembled the age-dependent alteration of SOD1 solubility in mutant H46R SOD1 transgenic mice. In contrast, overexpression of Hsp70 reduced the levels of SDS-dissociable soluble mutant H46R SOD1 monomers and SDS-stable soluble dimers. These findings indicate that SDS-dissociable soluble mutant SOD1 monomers and SDS-stable soluble dimers are degraded by the proteasome pathway and are modulated by molecular chaperones as misfolded intermediates. The previous in vitro study showed that a normal homodimer of SOD1 dissociates to an aggregation-prone monomeric intermediate by oxidation [32]. Further experiments would be necessary to see how potentially aggregation-promoting modifications, such as oxidation and nitration, relate to the alteration of SOD1 solubility.

Several reports showed that Hsp70 and its co-chaperone Hsp40 were involved in the aggregation process or the degradation of SOD1 [11,33], and Hsp70 and Hsp40 suppress SOD1 aggregate formation and improve neurite outgrowth [34]. Although in the previous report up-regulation of Hsp70 was not observed in the spinal cords of mutant SOD1 transgenic mice in contrast to cultured cells overexpressing mutant SOD1 [23], we found that the levels of Hsp70 and Hsp40 in mutant SOD1 transgenic mice increased in the SDS-soluble fraction before disease onset. This observation is consistent with the report that Hsp70 interacts with detergent-insoluble SOD1 rather than detergent-soluble SOD1 in cells [33]. However, it should be noted that endogenous Hsp70 and Hsp40 in the SDS-soluble fraction do not suppress accumulation of insoluble mutant SOD1 in the present H46R SOD1 transgenic mice. Furthermore, Liu et al. [35] showed that elevation of Hsp70 does not affect ALS disease onset and survival in several types of mutant SOD1 transgenic mice co-overexpressing Hsp70 at ~10-fold higher levels than control mice, suggesting that there was no benefit from chronically elevated Hsp70. In cells, overexpression of Hsp70 reduced the levels of SDS-soluble and SDS-insoluble mutant H46R SOD1, whereas it did not lead to the elevation of PBS-soluble and TX-soluble SOD1 levels. This result implies that overexpression of Hsp70 had an effect on the levels of mutant-specific insoluble SOD1 species by forwarding them to the degradation pathway rather than refolding them to a normal soluble pool of SOD1. Adachi et al. [36] reported that overexpression of Hsp70 decreased soluble monomeric androgen receptor (AR) protein in addition to HMW mutant AR protein in double transgenic mice expressing mutant AR protein and Hsp70, suggesting that Hsp70 enhanced mutant AR degradation. Since inhibition of the proteasome activity in cells had a strong effect on the accumulation of insoluble mutant SOD1 with up-regulation of endogenous Hsp70 and Hsp40, the discrepancy in beneficial effects of Hsp70 between cellular and mouse models of fALS may be explained by several possibilities. First, the diminishing of the proteasome activity may generate abundant misfolded proteins whose concentration exceeds the capacity of up-regulated endogenous Hsp70/40. Second, the main function of Hsp70 is to facilitate the proteasome pathway-dependent clearance of misfolded SOD1. Third, the accumulation of insoluble SOD1 species directly impairs the chaperone function of Hsp70 [37]. An approach for examining the toxicity of SDS-dissociable soluble mutant SOD1 monomers and SDS-stable soluble dimers may provide a clue to prevent a further accumulation of potentially toxic misfolded protein complexes in fALS.

Acknowledgments

This work was supported by Research Grants from the Japan ALS association (S.A.), a Grant-in-Aid for Scientific Research on Priority Areas (Advanced Brain Science Project) from the Ministry of Education, Culture, Sports, Science and Technology, Japan (S.A.), and a Research Grant on Measures for Intractable Diseases from the Ministry of Health, Labour and Welfare (T.K.).

References

[1] D.R. Rosen, T. Siddique, D. Patterson, D.A. Figlewicz, P. Sapp, A. Hentati, D. Donaldson, J. Goto, J.P. O'Regan, H.X. Deng, et al., Mutations in Cu/Zn superoxide dismutase gene are associated with familial amyotrophic lateral sclerosis, Nature 362 (1993) 59–62.
[2] M.E. Cudkowicz, D. McKenna-Yasek, P.E. Sapp, W. Chin, B. Geller, D.L. Hayden, D.A. Schoenfeld, B.A. Hosler, H.R. Horvitz, R.H. Brown, Epidemiology of mutations in superoxide dismutase in amyotrophic lateral sclerosis, Ann. Neurol. 41 (1997) 210–221.
[3] J.S. Valentine, P.J. Hart, Misfolded CuZnSOD and amyotrophic lateral sclerosis, Proc. Natl. Acad. Sci. USA 100 (2003) 3617–3622.
[4] A. Okado-Matsumoto, I. Fridovich, Subcellular distribution of superoxide dismutases (SOD) in rat liver: Cu,Zn-SOD in mitochondria, J. Biol. Chem. 276 (2001) 38388–38393.

[5] A.G. Reaume, J.L. Elliott, E.K. Hoffman, N.W. Kowall, R.J. Ferrante, D.F. Siwek, H.M. Wilcox, D.G. Flood, M.F. Beal, R.H. Brown Jr., R.W. Scott, W.D. Snider, Motor neurons in Cu/Zn superoxide dismutase-deficient mice develop normally but exhibit enhanced cell death after axonal injury, Nat. Genet. 13 (1996) 43–47.

[6] M.E. Gurney, H. Pu, A.Y. Chiu, M.C. Dal Canto, C.Y. Polchow, D.D. Alexander, J. Caliendo, A. Hentati, Y.W. Kwon, H.X. Deng, et al., Motor neuron degeneration in mice that express a human Cu,Zn superoxide dismutase mutation, Science 264 (1994) 1772–1775.

[7] M.E. Ripps, G.W. Huntley, P.R. Hof, J.H. Morrison, J.W. Gordon, Transgenic mice expressing an altered murine superoxide dismutase gene provide an animal model of amyotrophic lateral sclerosis, Proc. Natl. Acad. Sci. USA 92 (1995) 689–693.

[8] P.C. Wong, C.A. Pardo, D.R. Borchelt, M.K. Lee, N.G. Copeland, N.A. Jenkins, S.S. Sisodia, D.W. Cleveland, D.L. Price, An adverse property of a familial ALS-linked SOD1 mutation causes motor neuron disease characterized by vacuolar degeneration of mitochondria, Neuron 14 (1995) 1105–1116.

[9] L.I. Bruijn, M.W. Becher, M.K. Lee, K.L. Anderson, N.A. Jenkins, N.G. Copeland, S.S. Sisodia, J.D. Rothstein, D.R. Borchelt, D.L. Price, D.W. Cleveland, ALS-linked SOD1 mutant G85R mediates damage to astrocytes and promotes rapidly progressive disease with SOD1-containing inclusions, Neuron 18 (1997) 327–338.

[10] N. Shibata, A. Hirano, M. Kobayashi, T. Siddique, H.X. Deng, W.Y. Hung, T. Kato, K. Asayama, Intense superoxide dismutase-1 immunoreactivity in intracytoplasmic hyaline inclusions of familial amyotrophic lateral sclerosis with posterior column involvement, J. Neuropathol. Exp. Neurol. 55 (1996) 481–490.

[11] M. Watanabe, M. Dykes-Hoberg, V.C. Culotta, D.L. Price, P.C. Wong, J.D. Rothstein, Histological evidence of protein aggregation in mutant SOD1 transgenic mice and in amyotrophic lateral sclerosis neural tissues, Neurobiol. Dis. 8 (2001) 933–941.

[12] P.A. Jonsson, K. Ernhill, P.M. Andersen, D. Bergemalm, T. Brannstrom, O. Gredal, P. Nilsson, S.L. Marklund, Minute quantities of misfolded mutant superoxide dismutase-1 cause amyotrophic lateral sclerosis, Brain 127 (2004) 73–88.

[13] H.D. Durham, J. Roy, L. Dong, D.A. Figlewicz, Aggregation of mutant Cu/Zn superoxide dismutase proteins in a culture model of ALS, J. Neuropathol. Exp. Neurol. 56 (1997) 523–530.

[14] T. Koide, S. Igarashi, K. Kikugawa, R. Nakano, T. Inuzuka, M. Yamada, H. Takahashi, S. Tsuji, Formation of granular cytoplasmic aggregates in COS7 cells expressing mutant Cu/Zn superoxide dismutase associated with familial amyotrophic lateral sclerosis, Neurosci. Lett. 257 (1998) 29–32.

[15] M. Nagai, M. Aoki, I. Miyoshi, M. Kato, P. Pasinelli, N. Kasai, R.H. Brown Jr., Y. Itoyama, Rats expressing human cytosolic copper-zinc superoxide dismutase transgenes with amyotrophic lateral sclerosis: associated mutations develop motor neuron disease, J. Neurosci. 21 (2001) 9246–9254.

[16] J.A. Johnston, M.J. Dalton, M.E. Gurney, R.R. Kopito, Formation of high molecular weight complexes of mutant Cu, Zn-superoxide dismutase in a mouse model for familial amyotrophic lateral sclerosis, Proc. Natl. Acad. Sci. USA 97 (2000) 12571–12576.

[17] K. Puttaparthi, C. Wojcik, B. Rajendran, G.N. DeMartino, J.L. Elliott, Aggregate formation in the spinal cord of mutant SOD1 transgenic mice is reversible and mediated by proteasomes, J. Neurochem. 87 (2003) 851–860.

[18] J. Wang, G. Xu, D.R. Borchelt, High molecular weight complexes of mutant superoxide dismutase 1: age-dependent and tissue-specific accumulation, Neurobiol. Dis. 9 (2002) 139–148.

[19] M. Urushitani, J. Kurisu, K. Tsukita, R. Takahashi, Proteasomal inhibition by misfolded mutant superoxide dismutase 1 induces selective motor neuron death in familial amyotrophic lateral sclerosis, J. Neurochem. 83 (2002) 1030–1042.

[20] S. Tobisawa, Y. Hozumi, S. Arawaka, S. Koyama, M. Wada, M. Nagai, M. Aoki, Y. Itoyama, K. Goto, T. Kato, Mutant SOD1 linked to familial amyotrophic lateral sclerosis, but not wild-type SOD1, induces ER stress in COS7 cells and transgenic mice, Biochem. Biophys. Res. Commun. 303 (2003) 496–503.

[21] D.H. Hyun, M. Lee, B. Halliwell, P. Jenner, Proteasomal inhibition causes the formation of protein aggregates containing a wide range of proteins, including nitrated proteins, J. Neurochem. 86 (2003) 363–373.

[22] E. Kabashi, J.N. Agar, D.M. Taylor, S. Minotti, H.D. Durham, Focal dysfunction of the proteasome: a pathogenic factor in a mouse model of amyotrophic lateral sclerosis, J. Neurochem. 89 (2004) 1325–1335.

[23] W. Bruening, J. Roy, B. Giasson, D.A. Figlewicz, W.E. Mushynski, H.D. Durham, Up-regulation of protein chaperones preserves viability of cells expressing toxic Cu/Zn-superoxide dismutase mutants associated with amyotrophic lateral sclerosis, J. Neurochem. 72 (1999) 693–699.

[24] C.A. Ross, M.A. Poirier, Protein aggregation and neurodegenerative disease, Nat. Med. 10 (Suppl.) (2004) S10–S17.

[25] A.A. Michels, B. Kanon, A.W. Konings, K. Ohtsuka, O. Bensaude, H.H. Kampinga, Hsp70 and Hsp40 chaperone activities in the cytoplasm and the nucleus of mammalian cells, J. Biol. Chem. 272 (1997) 33283–33289.

[26] Y. Kobayashi, A. Kume, M. Li, M. Doyu, M. Hata, K. Ohtsuka, G. Sobue, Chaperones Hsp70 and Hsp40 suppress aggregate formation and apoptosis in cultured neuronal cells expressing truncated androgen receptor protein with expanded polyglutamine tract, J. Biol. Chem. 275 (2000) 8772–8778.

[27] S. Arawaka, H. Hasegawa, A. Tandon, C. Janus, F. Chen, G. Yu, K. Kikuchi, S. Koyama, T. Kato, P.E. Fraser, P. St. George-Hyslop, The levels of mature glycosylated nicastrin are regulated and correlate with gamma-secretase processing of amyloid beta-precursor protein, J. Neurochem. 83 (2002) 1065–1071.

[28] R. Chang-Hong, M. Wada, S. Koyama, H. Kimura, S. Arawaka, T. Kawanami, K. Kurita, T. Kadoya, M. Aoki, Y. Itoyama, T. Kato, Neuroprotective effect of oxidized galectin-1 in a transgenic mouse model of amyotrophic lateral sclerosis, Exp. Neurol. 194 (2005) 203–211.

[29] C.J. Epstein, K.B. Avraham, M. Lovett, S. Smith, O. Elroy-Stein, G. Rotman, C. Bry, Y. Groner, Transgenic mice with increased Cu/Zn-superoxide dismutase activity: animal model of dosage effects in Down syndrome, Proc. Natl. Acad. Sci. USA 84 (1987) 8044–8048.

[30] H. Fujiwara, M. Hasegawa, N. Dohmae, A. Kawashima, E. Masliah, M.S. Goldberg, J. Shen, K. Takio, T. Iwatsubo, alpha-Synuclein is phosphorylated in synucleinopathy lesions, Nat. Cell. Biol. 4 (2002) 160–164.

[31] P.J. Kahle, M. Neumann, L. Ozmen, V. Muller, S. Odoy, N. Okamoto, H. Jacobsen, T. Iwatsubo, J.Q. Trojanowski, H. Takahashi, K. Wakabayashi, N. Bogdanovic, P. Riederer, H.A. Kretzschmar, C. Haass, Selective insolubility of alpha-synuclein in human Lewy body diseases is recapitulated in a transgenic mouse model, Am. J. Pathol. 159 (2001) 2215–2225.

[32] R. Rakhit, J.P. Crow, J.R. Lepock, L.H. Kondejewski, N.R. Cashman, A. Chakrabartty, Monomeric Cu,Zn-superoxide dismutase is a common misfolding intermediate in the oxidation models of sporadic and familial amyotrophic lateral sclerosis, J. Biol. Chem. 279 (2004) 15499–15504.

[33] G.A. Shinder, M.C. Lacourse, S. Minotti, H.D. Durham, Mutant Cu/Zn-superoxide dismutase proteins have altered solubility and interact with heat shock/stress proteins in models of amyotrophic lateral sclerosis, J. Biol. Chem. 276 (2001) 12791–12796.

[34] H. Takeuchi, Y. Kobayashi, T. Yoshihara, J. Niwa, M. Doyu, K. Ohtsuka, G. Sobue, Hsp70 and Hsp40 improve neurite outgrowth and suppress intracytoplasmic aggregate formation in cultured neuronal cells expressing mutant SOD1, Brain Res. 949 (2002) 11–22.

[35] J. Liu, L.A. Shinobu, C.M. Ward, D. Young, D.W. Cleveland, Elevation of the Hsp70 chaperone does not effect toxicity in mouse

models of familial amyotrophic lateral sclerosis, J. Neurochem. 93 (2005) 875–882.
[36] H. Adachi, M. Katsuno, M. Minamiyama, C. Sang, G. Pagoulatos, C. Angelidis, M. Kusakabe, A. Yoshiki, Y. Kobayashi, M. Doyu, G. Sobue, Heat shock protein 70 chaperone overexpression ameliorates phenotypes of the spinal and bulbar muscular atrophy transgenic mouse model by reducing nuclear-localized mutant androgen receptor protein, J. Neurosci. 23 (2003) 2203–2211.
[37] H. Tummala, C. Jung, A. Tiwari, C.M. Higgins, L.J. Hayward, Z. Xu, Inhibition of chaperone activity is a shared property of several Cu,Zn-superoxide dismutase mutants that cause amyotrophic lateral sclerosis, J. Biol. Chem. 280 (2005) 17725–17731.

nature medicine

Conditional ablation of Stat3 or Socs3 discloses a dual role for reactive astrocytes after spinal cord injury

Seiji Okada[1–3], Masaya Nakamura[4], Hiroyuki Katoh[4], Tamaki Miyao[1], Takuya Shimazaki[1], Ken Ishii[4], Junichi Yamane[1,4], Akihiko Yoshimura[5], Yukihide Iwamoto[2], Yoshiaki Toyama[4] & Hideyuki Okano[1,3]

In the injured central nervous system (CNS), reactive astrocytes form a glial scar and are considered to be detrimental for axonal regeneration, but their function remains elusive. Here we show that reactive astrocytes have a crucial role in wound healing and functional recovery by using mice with a selective deletion of the protein signal transducer and activator of transcription 3 (Stat3) or the protein suppressor of cytokine signaling 3 (Socs3) under the control of the *Nes* promoter-enhancer (*Nes-Stat3*$^{-/-}$, *Nes-Socs3*$^{-/-}$). Reactive astrocytes in *Nes-Stat3*$^{-/-}$ mice showed limited migration and resulted in markedly widespread infiltration of inflammatory cells, neural disruption and demyelination with severe motor deficits after contusive spinal cord injury (SCI). On the contrary, we observed rapid migration of reactive astrocytes to seclude inflammatory cells, enhanced contraction of lesion area and notable improvement in functional recovery in *Nes-Socs3*$^{-/-}$ mice. These results suggest that Stat3 is a key regulator of reactive astrocytes in the healing process after SCI, providing a potential target for intervention in the treatment of CNS injury.

Because the regenerative capability of the mammalian CNS is poor, limited functional recovery occurs during the chronic phase of SCI. At the subacute phase of SCI, however, gradual functional recovery is observed to some extent in both rodents and humans (except in cases of complete paralysis). The mechanism behind this functional recovery remains unclear. Here, we investigated this issue by focusing on the action of reactive astrocytes in a mouse model of SCI.

To interpret the process of paralysis improvement in the subacute phase, we examined serial histological sections of contused spinal cords and followed motor function for 6 weeks after injury in wild-type mice and found that the area of neural cell loss gradually enlarged in a rostral-caudal direction within a few days after SCI (acute phase) and a portion of Hu-expressing neurons were positive for cleaved caspase-3, indicating that the secondary injury process lasted for several days in this model (**Supplementary Fig. 1** online) during which we observed limited functional recovery (**Fig. 1a**). Astrocytes surrounding the lesion underwent a typical change of hypertrophy, process extension and increased expression of intermediate filaments such as GFAP and Nestin by 7 d after SCI (**Fig. 1b**), characteristic of 'reactive astrocytes.' Notably, these astrocytes eventually migrated centripetally to the lesion epicenter and gradually compacted the CD11b^{+} inflammatory cells, contracting the lesion area up until 14 d after SCI (subacute phase; **Fig. 1c,d**). During this process, we observed repair of injured tissue and gradual functional improvement, and reactive astrocytes formed a physical barrier against inflammatory cells, commonly referred to as glial scar. After the migration of reactive astrocytes and completion of glial scar (reactive gliosis), functional improvement reached a plateau around 2 weeks after injury (**Fig. 1a,c**). Although the glial scar has a crucial part in the lack of axonal regeneration in the chronic phase of SCI[1], our data strongly suggest that the emergence and migration of reactive astrocytes have a prominent role in the repair of injured tissue and the restoration of motor function in the subacute phase (before completion of the glial scar).

To confirm that the compaction of the lesion results from migration and not from proliferation of reactive astrocytes, we labeled proliferating cells with bromodeoxyuridine (BrdU). Analysis of mice that received a single injection of BrdU at 7 d after SCI showed that the population of BrdU^{+} cells was composed of reactive astrocytes and inflammatory cells, which were gradually compacted to the lesion center as time progressed (**Fig. 1e** and **Supplementary Fig. 2** online). Analysis of mice that received daily injections of BrdU showed limited astrocyte proliferation after 7 d postinjury, suggesting that the development of reactive gliosis is mainly brought about by cellular hypertrophy and upregulation of GFAP of the astrocytes surrounding the lesion (**Fig. 1f,g**).

To address the regulatory mechanisms behind the reactive response of astrocytes, we investigated the role of Stat3 signaling (**Figs. 2** and **3**). Stat3 is a principal mediator in a variety of biological processes[2–4] including cancer progression, wound healing and the movement of various types of cells. In addition, Stat3 mediates certain aspects of astrogliosis downstream of the action of cytokines such as interleukin (IL)-6, leukemia inhibitory factor (LIF) and ciliary neurotrophic factor (CNTF) after CNS injury[5–8].

[1]Department of Physiology, Keio University School of Medicine, 35 Shinanomachi, Shinjuku-ku, Tokyo 160-8582, Japan. [2]Department of Orthopaedic Surgery, Graduate School of Medical Sciences, Kyushu University, 3-1-1 Maidashi, Higashi-ku, Fukuoka 812-8582, Japan. [3]Core Research for Evolutional Science and Technology (CREST), Japan Science and Technology, 4-1-8 Honcho, Kawaguchi, Saitama 332-0012, Japan. [4]Department of Orthopaedic Surgery, Keio University School of Medicine, 35 Shinanomachi, Shinjuku-ku, Tokyo 160-8582, Japan. [5]Division of Molecular and Cellular Immunology, Medical Institute of Bioregulation Graduate School of Medical Sciences, Kyushu University, 3-1-1 Maidashi, Higashi-ku, Fukuoka 812-8582, Japan. Correspondence should be addressed to H.O. (hidokano@sc.itc.keio.ac.jp).

Received 8 November 2005; accepted 28 April 2006; published online 18 June 2006; doi:10.1038/nm1425

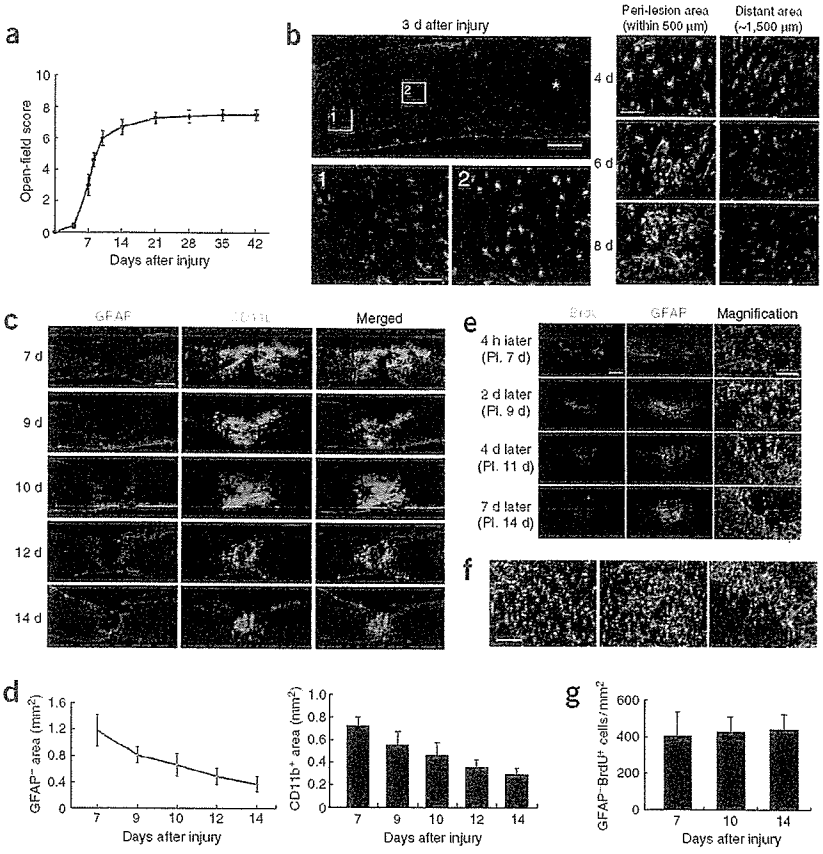

Figure 1 Migration of reactive astrocytes and compaction of inflammatory cells in wild-type mice. (**a**) Time course of lower limb functional recovery after SCI ($n = 10$). There was gradual recovery in the subacute phase. Data are mean ± s.e.m. (**b**) Phosphorylated Stat3 (green) and morphological changes were observed in GFAP$^+$ astrocytes (red) close to the lesion (boxed area 2) but not in distant areas (boxed area 1) at 3, 4, 6 and 8 d after SCI. Scale bar, 500 μm (upper left panel), 100 μm (lower left panel) and 50 μm (right panels). Asterisk indicates the lesion epicenter. (**c**) Time course of GFAP$^+$ reactive astrocytes and CD11b$^+$ cells. Reactive astrocytes gradually confine the area of inflammatory cell infiltration. Scale bar, 500 μm. (**d**) Quantitative analysis of GFAP$^-$ area (surrounded by reactive astrocytes) and CD11b$^+$ area ($n = 3$ per each time point). Data are mean ± s.d. (**e**) BrdU-labeled cells migrated toward the lesion epicenter. Mice were injected with BrdU (100 μg/g body weight) at 7 d after injury and killed 4 h, 2 d, 4 d, 7 d later. Scale bar, 500 μm and 100 μm. (**f**) The proliferating reactive astrocytes were labeled by daily injection of BrdU from the day of injury till killing at 7 (left), 10 (middle) and 14 d (right) after injury. GFAP, red; BrdU, green. Scale bar, 100 μm. (**g**) There were no differences in the number of GFAP$^+$BrdU$^+$ cells from 7 to 14 d after injury ($n = 3$ per group). Data are mean ± s.d.

In the injured spinal cord, phosphorylated Stat3 prominently increased at 12 h after injury, which remained detectable for 2 weeks (**Fig. 3a**). We observed phosphorylation and nuclear translocation of Stat3 mainly in reactive astrocytes surrounding the lesion, but not in distant areas for several days after injury (**Fig. 1b** and **Supplementary Fig. 1**). To elucidate the role of Stat3 in reactive astrocytes, we selectively disrupted the *Stat3* gene under the control of *Nes* gene promoter and second intronic enhancer, which are activated in reactive astrocytes after SCI[9,10]. We created conditional knockout mice (*Nes-Stat3*$^{-/-}$) by crossing *Stat3*^{loxP} mice[11] with *Nes*-Cre transgenic mice[12], as embryonic lethality ensues in Stat3-null mice. *Nes-Stat3*$^{-/-}$ mice showed no apparent abnormalities in motor function and development, although they showed signs of hyperphagia and leptin resistance[13]. To identify the cells that underwent Cre-mediated recombination, we crossed another transgenic line[14] carrying a reporter gene construct, *CAG* promoter-*lox*P-CAT-*lox*P-EGFP (CAG-CAT$^{loxP/loxP}$-EGFP), which directs the expression of EGFP upon Cre-mediated recombination. After SCI, we observed high Cre-mediated expression of EGFP from reactive astrocytes surrounding the lesion, but not from neurons or oligodendrocytes (**Supplementary Figs. 3** and **4** online), indicating recombination only in reactive astrocytes in both littermates and *Nes-Stat3*$^{-/-}$ mice.

At 2 weeks after injury, *Nes-Stat3*$^{-/-}$ mice showed markedly widespread infiltration of CD11b$^+$ inflammatory cells and demyelination compared to wild-type littermates (**Fig. 2a**). Notably, although the development of glial scar was observed around the injury site several days after injury in *Nes-Stat3*$^{-/-}$ mice (**Fig. 2a,b** and **Supplementary Fig. 3**), the configuration of these cells remained relatively unchanged for the following 6 weeks owing to their limited migration, resulting in widespread demyelination and severe motor deficits (**Fig. 2**). Quantifications of GFAP$^-$ area and CD11b$^+$ area in wild-type littermates and *Nes-Stat3*$^{-/-}$ mice were comparable at 7 d after injury, implying a similar degree of astrocyte loss owing to secondary injury, but marked differences developed during the following 7 d, suggesting that Stat3 has a large impact on the migration of astrocytes rather than their survival after SCI (**Fig. 2c**). The progressive compaction of GFAP$^+$EGFP$^+$ cells toward the lesion center observed in wild-type littermates did not occur in *Nes-Stat3*$^{-/-}$ mice, providing further evidence of Stat3-dependent migration of reactive astrocytes (**Fig. 2d**). Confocal imaging confirmed the emergence of reactive astrocytes without phosphorylated Stat3 in *Nes-Stat3*$^{-/-}$ mice (**Fig. 2e**), indicating that the Stat3 activation is not necessarily indispensable for the appearance of reactive astrocytes or for the upregulation of *Gfap* and *Nes*. These data suggest that Stat3 is a key molecule for the migratory function of reactive astrocytes, which may be deeply involved in tissue repair and functional recovery after SCI (**Fig. 2**).

To further investigate the relationship between Stat3 signaling and function of reactive astrocytes, we analyzed SCI in *Nes-Socs3*$^{-/-}$ mice[15]. Socs3 is the negative feedback molecule of Stat3 and the 'bipolar' relationship between Stat3 and Socs3 has been noted in several selective deletion experiments[13,15,16]. In the injured spinal cord of *Nes-Socs3*$^{-/-}$ mice, phosphorylation of Stat3 was significantly greater and prolonged compared to that in wild-type mice, and immunohistochemistry confirmed greater expression of phosphorylated Stat3 in reactive astrocytes (**Fig. 3a–c**). Notably, the rapid development of reactive gliosis that compacted inflammatory cells in the injured spinal cord of *Nes-Socs3*$^{-/-}$ mice was observed as early as 7 d after injury (**Fig. 3d,e**). GFAP$^-$ area and CD11b$^+$ area were significantly reduced in *Nes-Socs3*$^{-/-}$ mice at 7 d after injury, during which *Nes-Socs3*$^{-/-}$ mice showed marked improvement of motor function compared to littermates (**Fig. 3f,g**). The differences in the area between wild-type

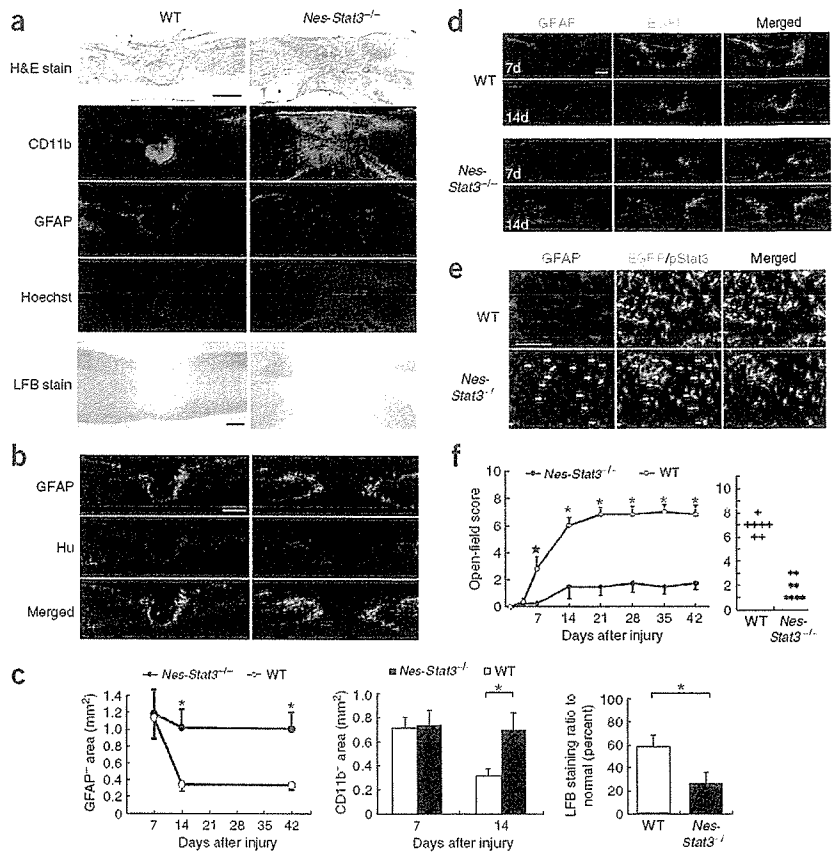

Figure 2 Compaction of inflammatory cells by reactive astrocytes and functional recovery were limited in *Nes-Stat3*$^{-/-}$ mice after SCI. (**a**) At 2 weeks after SCI, the infiltration of CD11b^{+} cells, GFAP^{-} area and demyelination were greater in *Nes-Stat3*$^{-/-}$ mice compared to wild-type (WT) littermates. Scale bars, 500 μm (upper left panel) and 300 μm (lower left panel). (**b**) The areas negative for Hu and GFAP were large in *Nes-Stat3*$^{-/-}$ mice even at 6 weeks after injury. Scale bar, 500 μm. (**c**) Comparison of GFAP^{-} area, CD11b^{+} area and LFB-positive area in both groups ($n = 3$ per each time point). Error bar indicates s.d. $^{*}P < 0.01$. (**d**) The location of GFAP^{+}EGFP^{+} reactive astrocytes shifted toward the lesion epicenter from 1 to 2 weeks in wild-type (WT) littermates, whereas their position remained relatively unchanged in *Nes-Stat3*$^{-/-}$ mice. Scale bar, 300 μm. (**e**) In *Nes-Stat3*$^{-/-}$ mice, Cre-mediated EGFP^{+} cells (green) were colocalized with GFAP^{+} reactive astrocytes (blue; arrows), but colocalization with phosphorylated Stat3 (red) was hardly observed at 4 d after injury. Scale bar, 100 μm. (**f**) Time course of functional recovery of lower limbs and the score of each mouse at 6 weeks after SCI. Whereas gradual recovery was observed in the subacute phase in wild-type (WT) littermates, little improvement was observed in *Nes-Stat3*$^{-/-}$ mice ($n = 7$ *Nes-Stat3*$^{-/-}$; $n = 8$ wild-type). Data are mean ± s.e.m. $^{*}P < 0.01$, $^{\star}P < 0.05$.

littermates and *Nes-Socs3*$^{-/-}$ mice became less pronounced at 2 weeks after injury, but *Nes-Socs3*$^{-/-}$ mice continually showed better motor function. Quantification of demyelination, oligodendrocyte-lost area and distal cord serotonergic innervation showed significant differences between the two groups (**Fig. 3f,h,i** and **Supplementary Fig. 4**). But GAP43^{+} regenerative fibers were comparable irrespective of genotype, and these fibers generally did not colocalize with 5HT^{+} fibers, indicating that the difference in serotonergic innervation did not result from regeneration (**Supplementary Fig. 5** online). These results suggest that the prompt contraction of the lesion spares more myelin, oligodendrocytes and serotonergic fibers, resulting in improved recovery.

Compared to wild-type mice, the development of reactive gliosis that secluded inflammatory cells was enhanced in *Nes-Socs3*$^{-/-}$ mice, whereas it was significantly delayed in *Nes-Stat3*$^{-/-}$ mice, indicating Stat3 signaling as an important factor in the developmental process of reactive gliosis after SCI (**Fig. 4a,b**).

Consistent with *in vivo* results, the *in vitro* migration behavior of astrocytes showed similar properties in a scratch-wounded assay that simulated the postinjury *in vivo* behavior of reactive astrocytes[17]. Astrocytes harvested from *Nes-Socs3*$^{-/-}$ mice showed a higher degree of migration, whereas impaired migration was observed in astrocytes of *Nes-Stat3*$^{-/-}$compared to wild-type mice (**Fig. 4c–e**). As proliferation rates among the three groups were comparable, cell migration activity was not dependent upon cell proliferation activity (data not shown).

A recent report indicates a possible molecular link between Stat3-zinc signaling and cell movement[18]. The zinc transporter LIV1, identified as the transcriptional downstream target of Stat3, was found to be essential for the nuclear localization of the zinc-finger protein Snail, a transcriptional repressor of the *Cdh1* gene (which encodes E-cadherin). Thus, the absence of Stat3 signaling causes dysregulation of cell adhesion and impairs cell movement. Strong support for this theory is given by the result that zinc deficiency impaired compaction of inflammatory cells by reactive astrocytes and increased the number of apoptotic cells after CNS injury[19]. In addition, CNS injury in knockout mice of metallothioneins (zinc-binding proteins involved in zinc ion regulation) had histological characteristics similar to *Nes-Stat3*$^{-/-}$ mice, such as impaired migratory behavior of reactive astrocytes, wide infiltration of inflammatory cells and severe impairment of wound healing[20]. On the other hand, astrocyte-targeted IL-6–expressing transgenic mice showed prompt migration of reactive astrocytes and compaction of inflammatory cells as well as substantial tissue repair after CNS injury[21] similar to *Nes-Socs3*$^{-/-}$ mice (though hyperactivation of IL-6 signaling without a specific cellular target caused considerably more damage owing to robust inflammation after CNS injury[6,22]). Here, expression of *Slc39a6* mRNA (encoding LIV1) in reactive astrocytes 5 d after injury was robust in wild-type mice but was limited in *Nes-Stat3*$^{-/-}$ mice. Consistent with *Slc39a6* mRNA expression, E-cadherin was expressed in reactive astrocytes of *Nes-Stat3*$^{-/-}$ but not in wild-type mice at 2 weeks after SCI. Furthermore, real-time RT-PCR of injured spinal cords showed differences in expression of *Scl39ac* mRNA among the three groups (**Fig. 4f–h**). These data provide insight into the mechanism of astrocytic migration through Stat3 signaling and indicate the significance of reactive astrocytes after CNS injury.

In our SCI model, the area of neuronal cell loss before the emergence of reactive astrocytes was comparable for wild-type and conditional knockout mice, suggesting that the effect of Stat3

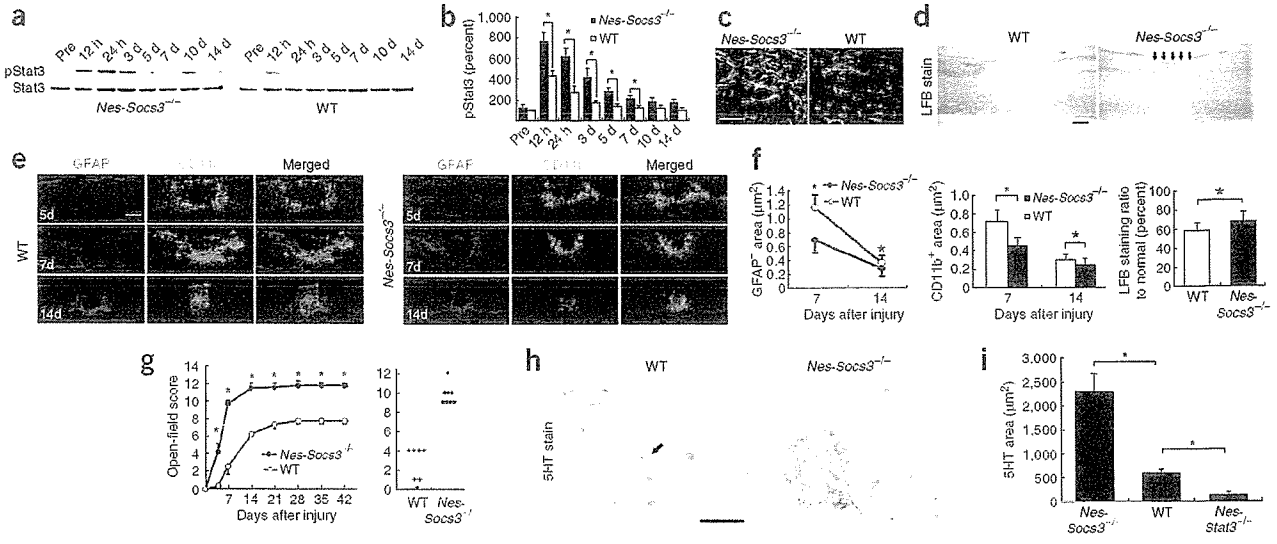

Figure 3 Enhanced activation of Stat3, prompt compaction of inflammatory cells and marked functional improvement in *Nes-Socs3*$^{-/-}$ mice. (**a**) Western blot analysis of Stat3 phosphorylation in injured spinal cord of wild-type (WT) and *Nes-Socs3*$^{-/-}$ mice. pStat3, phosphorylated Stat3. (**b**) Changes in the ratios of pStat3 to total Stat3 after SCI (mean ± s.e.m., $n = 4$ per group). $^{*}P < 0.05$. (**c**) Immunostaining of pStat3 and reactive astrocytes at 7 d after SCI. GFAP, red; pStat3, green. Scale bar, 100 μm. (**d**) Luxol Fast Blue (LFB) staining in littermates and *Nes-Socs3*$^{-/-}$ mice at 2 weeks after SCI. Arrows indicate the spared myelin in the dorsal part of the lesion epicenter. Scale bar, 300 μm. (**e**) Time course analysis of reactive astrocytes and CD11b^{+} cells. The early development of reactive astrocytes and compaction of inflammatory cells in *Nes-Socs3*$^{-/-}$ mice was visible as early as 7 d after SCI. Scale bar, 500 μm. (**f**) Quantitative analysis of GFAP^{-} area, CD11b^{+} area and LFB-positive area (mean ± s.d., $n = 4$). $^{*}P < 0.01$, $^{\star}P < 0.05$. (**g**) Time course of functional recovery and the score of each mouse at 7 d after SCI. Data are mean ± s.e.m. $^{*}P < 0.01$. (**h**) 5HT^{+} staining of the ventral horn distal to the lesion in wild-type (WT) littermates and *Nes-Socs3*$^{-/-}$ mice at 6 weeks after SCI. Arrow indicates spared 5HT^{+} fibers. Scale bar, 100 μm. (**i**) Quantitative analysis of serotonergic innervation of the distal cord in the three groups (mean ± s.e.m., $n = 4$ per each group). $^{*}P < 0.01$.

signaling on neuronal survival was minimal compared with its effect on the development and migration of reactive astrocytes (**Supplementary Fig. 1**).

The majority of studies on CNS injury have shown that the glial scar formed in part by reactive astrocytes hinders axonal regeneration. In mice lacking both GFAP and vimentin, reduced astroglial reactivity resulted in improved sprouting of axons and functional restoration after SCI[23]. But reactive astrocytes are also important for supporting repair of the blood-brain barrier. They prevent infiltration of CD45^{+} leukocytes and protect neurons and oligodendrocytes as shown by the selective ablation of dividing astrocytes using ganciclovir and GFAP-TK transgenic mice[24,25]. Here, we showed that Stat3 signaling in reactive astrocytes have a considerable role in the repair of injured tissue and the recovery of motor function. Although these results seem to conflict with one another, consideration of the timeframe in which these events were observed suggests a possible phase-dependent role of reactive astrocytes. In mice lacking both GFAP and vimentin, functional recovery was observed later than 2 weeks after injury[23], whereas substantial recovery was completed within 2 weeks after injury in *Nes-Stat3*$^{-/-}$ and *Nes-Socs3*$^{-/-}$ mice, suggesting that reactive astrocytes in the subacute phase repair tissue and restore function, whereas in the chronic phase of injury they impair axonal regeneration as a physical and chemical barrier.

Together, these results show that reactive astrocytes have a pivotal role in the repair of injured tissue and the recovery of motor function in the subacute phase after SCI, and that the function of reactive astrocytes is largely dependent on Stat3 signaling. This work also raises Stat3 signaling and reactive astrocytes as a potential new therapeutic target for the treatment of traumatic injury in CNS.

METHODS

Generation of conditional knockout mice. *Stat3*$^{loxP/loxP}$ mice, *Stat3*$^{loxP/-}$ mice, *Socs3*$^{loxP/loxP}$ mice, *Nes*-Cre mice and *CAG*-CAT$^{loxP/loxP}$–EGFP transgenic mice were as described elsewhere[3,11,12,14,15,26]. To generate *Nes-Stat3*$^{-/-}$ or *Nes-Socs3*$^{-/-}$ mice, we crossed *Nes*-Cre mice with *Stat3*$^{loxP/loxP}$, *Stat3*$^{loxP/-}$ mice[3,26] or *Socs3*$^{loxP/loxP}$ mice[15]. We used wild-type littermates (*Stat3*$^{loxP/loxP}$ or *Socs3*$^{loxP/loxP}$) as controls in histological and functional evaluations. We performed genotyping with primers described elsewhere[3,12,14,15]. All mice were housed in a temperature- and humidity-controlled environment on a 12-h light-dark cycle.

SCI model. We anesthetized adult C57BL/6J mice, wild-type littermates and conditional knockout mice (female, 8 weeks old) using an intraperitoneal injection of ketamine (100 mg/kg) and xylazine (10 mg/kg). After laminectomy at the tenth thoracic spinal vertebrae, we exposed the dorsal surface of the dura mater and induced SCI using a commercially available SCI device (60 kdyn using Infinite Horizon impactor, Precision Systems & Instrumentation) as previously described[27]. We evaluated motor function of the hind limbs with the locomotor rating test on the Basso-Beattie-Bresnahan (BBB) scale[28] for 6 weeks after injury. The obesity of *Nes-Stat3*$^{-/-}$ mice was not a problem in this study, because their functional recovery was limited to the point at which weight bearing was not an issue. All procedures were approved by the ethics committee of Keio University and were in accordance with the Guide for the Care and Use of Laboratory Animals (US National Institutes of Health).

Immunohistochemistry. We anesthetized mice and transcardially perfused them with 4% paraformaldehyde in 0.1 M PBS. We removed spinal cords, embedded them in OCT compound and sectioned them sagittally at 20 μm on a cryostat. We stained tissue sections with primary antibodies to GFAP (DAKO), cleaved caspase-3 (Cell Signaling), CD11b (a marker of monocyte/macrophages and granulocytes; MBL), BrdU (Chemicon), Nestin (Rat 401, Chemicon), GFP (MBL), phosphorylated Stat3 (Cell Signaling), GSTπ (BD Biosciences), serotonin (5HT; DiaSorin, Inc.), GAP43 (Chemicon), E-cadherin

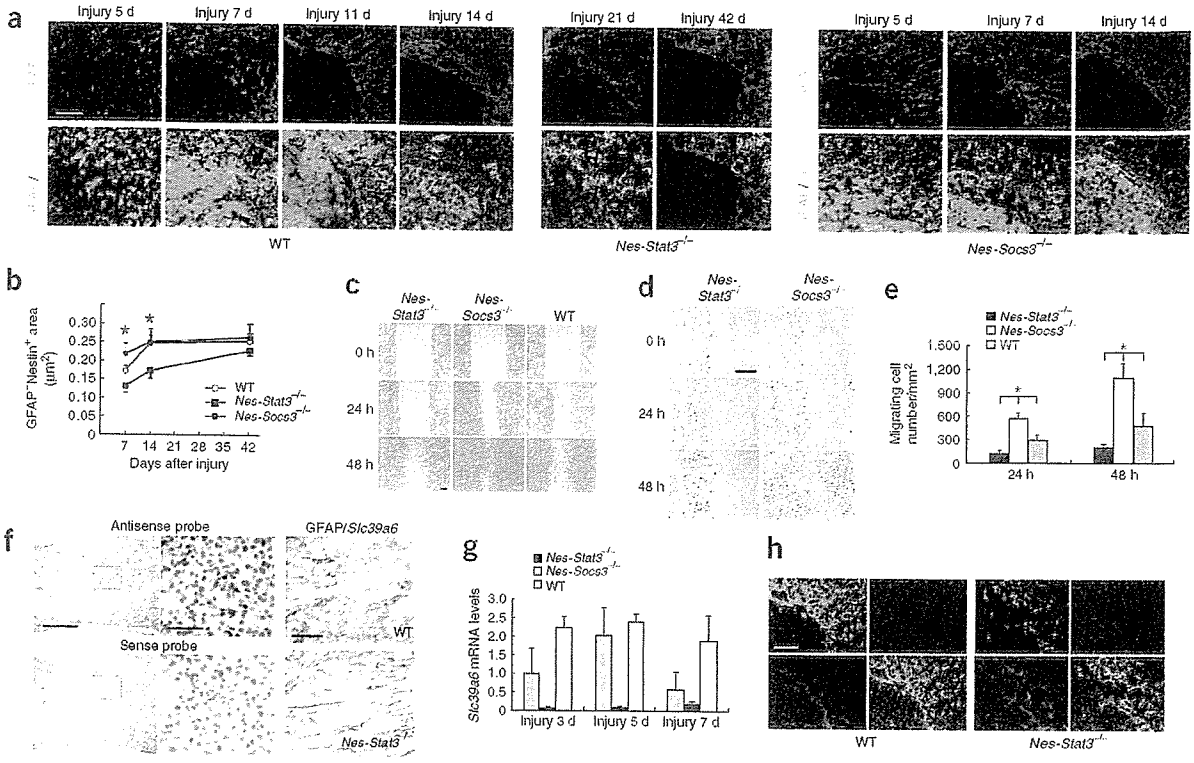

Figure 4 Involvement of Stat3 signaling in the development of reactive gliosis *in vivo*, the migration of reactive astrocytes *in vitro* and the transcriptional activity of LIV1. **(a)** Morphology of reactive astrocytes around the lesion area and infiltration of inflammatory cells in wild-type (WT), *Nes-Stat3*$^{-/-}$ and *Nes-Socs3*$^{-/-}$ mice. Scale bar, 100 μm. **(b)** The amount of reactive gliosis was measured as GFAP$^+$Nestin$^+$ (EGFP) area in the three groups ($n = 3$). Error bar indicates s.e.m. $^*P < 0.05$. **(c)** *In vitro* scratch injury of monolayer cultured astrocytes derived from wild-type (WT), *Nes-Stat3*$^{-/-}$ and *Nes-Socs3*$^{-/-}$ mice. Scale bar, 20 μm. **(d)** Magnified image of reactive astrocytes derived from *Nes-Stat3*$^{-/-}$ and *Nes-Socs3*$^{-/-}$ mice. Scale bar, 20 μm. **(e)** Migrating cells were quantified as mean number ± s.e.m. per millimeter squared beyond the wound edge ($n = 3$). $^*P < 0.01$. **(f)** *In situ* hybridization of *Slc39a6* mRNA in injured spinal cord. *Slc39a6* mRNA was observed in GFAP$^+$ reactive astrocytes in wild-type but was rarely found in *Nes-Stat3*$^{-/-}$ mice. Scale bars, 200 μm (upper left panel), 50 μm (upper middle panel) and 50 μm (upper right panel). **(g)** Expression of *Slc39a6* mRNA in injured spinal cords as determined by real-time RT-PCR in the three groups ($n = 3$). Each group was normalized to *Gapdh* values. There are significant differences ($P < 0.01$) among the three groups at each time point. Error bar indicates s.e.m. **(h)** Expression of E-cadherin (red) was not observed in reactive astrocytes of wild-type mice, whereas its active expression was observed in *Nes-Stat3*$^{-/-}$ mice at 2 weeks after SCI. GFAP, green; Hoechst stain, blue. Scale bar, 100 μm.

(Santa Cruz) and Hu[29] (a gift from R. Darnell, The Rockefeller University). We performed nuclear counterstaining with Hoechst 33342 (Molecular Probes). Images were obtained by fluorescence microscopy (Axioskop 2 Plus; Carl Zeiss) or confocal microscopy (LSM510; Carl Zeiss). To quantify the immunopositive and immunonegative area *in vivo*, we selected five representative midsagittal sections in each mouse and measured the area with the MCID system (Imaging Research, Inc.). We quantified the immunopositive area using grain counting and detected the immunonegative area by quantifying the dark area after image binarization. For myelin staining, we performed Luxol Fast Blue (LFB) stain. For comparison of LFB positive area, we selected five representative sagittal sections (3 mm long) of injured spinal cords (2 weeks after SCI) from positions 0.25 mm and 0.5 mm right of the midline, at the midline, and 0.25 mm and 0.5 mm left of the midline and LFB-positive area (blue area), and measured them by MCID system (grain counting), and calculated the ratio to normal section. To count GFAP$^+$BrdU$^+$ cells, we selected five representative sagittal sections and randomly captured six regions in each section at ×200 magnification by confocal microscopy. For quantification of 5HT$^+$ fibers, we randomly captured ten regions in each axial section of distal cord at ×200 magnification, and we quantified the total 5HT$^+$ area using the MCID system. We maintained light intensity and threshold values at constant levels for all analyses. In all sagittal sections shown here, the left side is rostral.

***In vitro* migration assay.** We prepared primary astrocytes from 2-d-old wild-type and conditional knockout mice as previously described[30]. After several passages in DMEM with 10% FBS, we trypsinized cells and plated them to confluency on coverslips coated with poly-L-lysine. After reaching subconfluency, we treated cells with 10 μg/ml mitomycin C for 2 h to avoid the effects of cell proliferation and then subjected them to scratching. We created a cell-free area by scratching the monolayer with a pipette tip and evaluated the migration of cells to the cell-free area from the surrounding area at 24 h and 48 h. We counted the number of migrating astrocytes after taking photographs of ten nonoverlapping fields.

Western blotting. We anesthetized SCI mice, transcardially perfused them with saline, and isolated and lysed a 4-mm long section of the injured spinal cord. We resolved lysates with SDS-PAGE and immunoblotted membranes with antibody to phosphorylated Stat3 (Tyr705) and antibody to Stat3 (Cell Signaling).

***In situ* hybridization.** For detection of *Slc39a6* mRNA, we subcloned a 774-bp DNA fragment corresponding to the nucleotide positions 331–1104 of mouse Slc39a6 into pGEMT-Easy vector (Promega) and used it to generate sense or antisense RNA probes. We hybridized paraffin-embedded spinal cord sections (6 μm) with digoxigenin-labeled RNA probes at 60 °C for 16 h. We detected the bound label using NBT-BCIP, an alkaline phosphate color substrate. We counterstained sections with Kernechtrot.

Real-time quantitative PCR. We isolated total RNA from the injured spinal cord (4 mm long) using the RNeasy Kit (Qiagen) and obtained cDNA by

reverse transcriptase reaction. For quantitative analysis of *Slc39a6* mRNA expression, we used the cDNA as a template in a TaqMan real-time PCR assay using the ABI Prism 7000 sequence detection system (Applied Biosystems) according to the manufacturer's protocol. We performed the amplification using the following primers: forward primer, 5′-TGAAGGCAGCACCAATAG CA-3′; reverse primer, 5′-GGCCTGGATGGTGATCATG-3′; and TaqMan probe, 5′-FAM-CGTCACTGAAATTGTGCAGCCCGTC-TAMRA-3′.

Statistical analysis. We performed statistical analysis with an unpaired two-tailed Student *t*-test for single comparisons, and ANOVA followed by the Tukey-Kramer test for multiple comparisons. For the open-field score, we used repeated-measures ANOVA and the Mann-Whitney *U*-test. In all statistical analyses, significance was accepted at $P < 0.05$.

Accession codes. GenBank: *Mus musculus* solute carrier family 39 (metal ion transporter) number 6 (Slc39a6), NM_139143.

Note: Supplementary information is available on the Nature Medicine website.

ACKNOWLEDGMENTS

This work was supported by grants from Ministry of Education, Culture, Sports, Science and Technology (MEXT), Japan, the General Insurance Association in Japan, Terumo Foundation Life Science Foundation (to H.O.), and a Grant-in-Aid for the 21st century COE program, Keio Gijuku Academic Development Funds.

AUTHOR CONTRIBUTIONS

S.O. performed most of the experiments to characterize mouse phenotypes. M.N. instructed group members about experimental processes. H.K. helped prepare the manuscript. T.M. and T.S. maintained and prepared knockout mice. K.I. and J.Y. prepared spinal cord–injured animals. A.Y. provided *Nes-Socs3*$^{-/-}$ mice. Y.I. advised experiments by S.O. Y.T. and H.O. designed experiments and prepared the manuscript.

COMPETING INTERESTS STATEMENT

The authors declare that they have no competing financial interests.

Published online at http://www.nature.com/naturemedicine/
Reprints and permissions information is available online at http://npg.nature.com/reprintsandpermissions/

1. Silver, J. & Miller, J.H. Regeneration beyond the glial scar. *Nat. Rev. Neurosci.* **5**, 146–156 (2004).
2. Wang, T. *et al.* Regulation of the innate and adaptive immune responses by Stat-3 signaling in tumor cells. *Nat. Med.* **10**, 48–54 (2004).
3. Sano, S. *et al.* Keratinocyte-specific ablation of Stat3 exhibits impaired skin remodeling, but does not affect skin morphogenesis. *EMBO J.* **18**, 4657–4668 (1999).
4. Hirano, T., Ishihara, K. & Hibi, M. Roles of STAT3 in mediating the cell growth, differentiation and survival signals relayed through the IL-6 family of cytokine receptors. *Oncogene* **19**, 2548–2556 (2000).
5. Sriram, K., Benkovic, S.A., Hebert, M.A., Miller, D.B. & O'Callaghan, J.P. Induction of gp130-related cytokines and activation of JAK2/STAT3 pathway in astrocytes precedes up-regulation of glial fibrillary acidic protein in the 1-methyl-4-phenyl-1,2,3,6-tetrahydropyridine model of neurodegeneration: key signaling pathway for astrogliosis *in vivo*? *J. Biol. Chem.* **279**, 19936–19947 (2004).
6. Kerr, B.J. & Patterson, P.H. Potent pro-inflammatory actions of leukemia inhibitory factor in the spinal cord of the adult mouse. *Exp. Neurol.* **188**, 391–407 (2004).
7. Xia, X.G., Hofmann, H.D., Deller, T. & Kirsch, M. Induction of STAT3 signaling in activated astrocytes and sprouting septal neurons following entorhinal cortex lesion in adult rats. *Mol. Cell. Neurosci.* **21**, 379–392 (2002).
8. Klein, M.A. *et al.* Impaired neuroglial activation in interleukin-6 deficient mice. *Glia* **19**, 227–233 (1997).
9. Frisen, J., Johansson, C.B., Torok, C., Risling, M. & Lendahl, U. Rapid, widespread, and longlasting induction of nestin contributes to the generation of glial scar tissue after CNS injury. *J. Cell Biol.* **131**, 453–464 (1995).
10. Johansson, C.B., Lothian, C., Molin, M., Okano, H. & Lendahl, U. Nestin enhancer requirements for expression in normal and injured adult CNS. *J. Neurosci. Res.* **69**, 784–794 (2002).
11. Takeda, K. *et al.* Stat3 activation is responsible for IL-6-dependent T cell proliferation through preventing apoptosis: generation and characterization of T cell-specific Stat3-deficient mice. *J. Immunol.* **161**, 4652–4660 (1998).
12. Betz, U.A., Vosshenrich, C.A., Rajewsky, K. & Muller, W. Bypass of lethality with mosaic mice generated by Cre-loxP-mediated recombination. *Curr. Biol.* **6**, 1307–1316 (1996).
13. Gao, Q. *et al.* Disruption of neural signal transducer and activator of transcription 3 causes obesity, diabetes, infertility, and thermal dysregulation. *Proc. Natl. Acad. Sci. USA* **101**, 4661–4666 (2004).
14. Kawamoto, S. *et al.* A novel reporter mouse strain that expresses enhanced green fluorescent protein upon Cre-mediated recombination. *FEBS Lett.* **470**, 263–268 (2000).
15. Mori, H. *et al.* Socs3 deficiency in the brain elevates leptin sensitivity and confers resistance to diet-induced obesity. *Nat. Med.* **10**, 739–743 (2004).
16. Kubo, M., Hanada, T. & Yoshimura, A. Suppressors of cytokine signaling and immunity. *Nat. Immunol.* **4**, 1169–1176 (2003).
17. Faber-Elman, A., Solomon, A., Abraham, J.A., Marikovsky, M. & Schwartz, M. Involvement of wound-associated factors in rat brain astrocyte migratory response to axonal injury: *in vitro* simulation. *J. Clin. Invest.* **97**, 162–171 (1996).
18. Yamashita, S. *et al.* Zinc transporter LIVI controls epithelial-mesenchymal transition in zebrafish gastrula organizer. *Nature* **429**, 298–302 (2004).
19. Penkowa, M., Giralt, M., Thomsen, P.S., Carrasco, J. & Hidalgo, J. Zinc or copper deficiency-induced impaired inflammatory response to brain trauma may be caused by the concomitant metallothionein changes. *J. Neurotrauma* **18**, 447–463 (2001).
20. Penkowa, M., Carrasco, J., Giralt, M., Moos, T. & Hidalgo, J. CNS wound healing is severely depressed in metallothionein I- and II-deficient mice. *J. Neurosci.* **19**, 2535–2545 (1999).
21. Penkowa, M. *et al.* Astrocyte-targeted expression of IL-6 protects the CNS against a focal brain injury. *Exp. Neurol.* **181**, 130–148 (2003).
22. Lacroix, S., Chang, L., Rose-John, S. & Tuszynski, M.H. Delivery of hyper-interleukin-6 to the injured spinal cord increases neutrophil and macrophage infiltration and inhibits axonal growth. *J. Comp. Neurol.* **454**, 213–228 (2002).
23. Menet, V., Prieto, M., Privat, A. & Gimenezy Ribotta, M. Axonal plasticity and functional recovery after spinal cord injury in mice deficient in both glial fibrillary acidic protein and vimentin genes. *Proc. Natl. Acad. Sci. USA* **100**, 8999–9004 (2003).
24. Bush, T.G. *et al.* Leukocyte infiltration, neuronal degeneration, and neurite outgrowth after ablation of scar-forming, reactive astrocytes in adult transgenic mice. *Neuron* **23**, 297–308 (1999).
25. Faulkner, J.R. *et al.* Reactive astrocytes protect tissue and preserve function after spinal cord injury. *J. Neurosci.* **24**, 2143–2155 (2004).
26. Ozawa, Y. *et al.* Downregulation of STAT3 activation is required for presumptive rod photoreceptor cells to differentiate in the postnatal retina. *Mol. Cell. Neurosci.* **26**, 258–270 (2004).
27. Scheff, S.W., Rabchevsky, A.G., Fugaccia, I., Main, J.A. & Lumpp, J.E., Jr. Experimental modeling of spinal cord injury: characterization of a force-defined injury device. *J. Neurotrauma* **20**, 179–193 (2003).
28. Basso, D.M., Beattie, M.S. & Bresnahan, J.C. Graded histological and locomotor outcomes after spinal cord contusion using the NYU weight-drop device versus transection. *Exp. Neurol.* **139**, 244–256 (1996).
29. Okano, H.J. & Darnell, R.B. A hierarchy of Hu RNA binding proteins in developing and adult neurons. *J. Neurosci.* **17**, 3024–3037 (1997).
30. Sanai, N. *et al.* Unique astrocyte ribbon in adult human brain contains neural stem cells but lacks chain migration. *Nature* **427**, 740–744 (2004).

WILEY InterScience® DISCOVER SOMETHING GREAT

Journal of Neuroscience Research 83:119–133 (2006)

Disease Progression of Human SOD1 (G93A) Transgenic ALS Model Rats

Arifumi Matsumoto,[1,3,6] Yohei Okada,[1,4,6] Masanori Nakamichi,[5] Masaya Nakamura,[2] Yoshiaki Toyama,[2] Gen Sobue,[4] Makiko Nagai,[3] Masashi Aoki,[3] Yasuto Itoyama,[3] and Hideyuki Okano[1,6]*

[1]Department of Physiology, Keio University School of Medicine, Tokyo, Japan
[2]Department of Orthopaedic Surgery, Keio University School of Medicine, Tokyo, Japan
[3]Department of Neurology, Tohoku University Graduate School of Medicine, Sendai, Japan
[4]Department of Neurology, Nagoya University Graduate School of Medicine, Nagoya, Japan
[5]Takeda Chemical Industries, Ltd., Osaka, Japan
[6]Core Research for Evolutional Science and Technology (CREST), Japan Science and Technology Agency (JST), Saitama, Japan

The recent development of a rat model of amyotrophic lateral sclerosis (ALS) in which the rats harbor a mutated human SOD1 (G93A) gene has greatly expanded the range of potential experiments, because the rats' large size permits biochemical analyses and therapeutic trials, such as the intrathecal injection of new drugs and stem cell transplantation. The precise nature of this disease model remains unclear. We described three disease phenotypes: the forelimb-, hindlimb-, and general-types. We also established a simple, non-invasive, and objective evaluation system using the body weight, inclined plane test, cage activity, automated motion analysis system (SCANET), and righting reflex. Moreover, we created a novel scale, the Motor score, which can be used with any phenotype and does not require special apparatuses. With these methods, we uniformly and quantitatively assessed the onset, progression, and disease duration, and clearly presented the variable clinical course of this model; disease progression after the onset was more aggressive in the forelimb-type than in the hindlimb-type. More importantly, the disease stages defined by our evaluation system correlated well with the loss of spinal motor neurons. In particular, the onset of muscle weakness coincided with the loss of approximately 50% of spinal motor neurons. This study should provide a valuable tool for future experiments to test potential ALS therapies.

Key words: amyotrophic lateral sclerosis; evaluation system; behavioral analyses; phenotype; variability

Amyotrophic lateral sclerosis (ALS) is a fatal neurodegenerative disorder that mainly affects the upper and lower motor neurons (de Belleroche et al., 1995). It is characterized by progressive muscle weakness, amyotrophy, and death from respiratory paralysis, usually within 3–5 years of onset (Brown 1995). Although most cases of ALS are sporadic (SALS), approximately 10% are familial (FALS) (Mulder et al., 1986). Moreover, 20–25% of FALS cases are due to mutations in the gene encoding copper-zinc superoxide dismutase (SOD1) (Deng et al., 1993; Rosen et al., 1993). More than 100 different mutations in the SOD1 gene have been identified in FALS so far.

Until recently, animal models of FALS have been various transgenic mice that express a mutant human SOD1 (hSOD1) gene. Of these, a transgenic mouse carrying the G93A (Gly-93 → Ala) mutant hSOD1 gene was the first described (Gurney et al., 1994) and is used all over the world because this model closely recapitulates the clinical and histopathological features of the human disease. To evaluate the therapeutic effects of potential ALS treatments in this animal, many motor-related behavioral tasks are used (Chiu et al., 1995; Barneoud et al., 1997; Garbuzova-Davis et al., 2002; Sun et al., 2002; Wang et al., 2002; Inoue et al., 2003; Kaspar et al., 2003; Weydt et al., 2003; Azzouz et al., 2004). However, transgenic mice have innate limitations for some types of experiments because of their small size.

Recently, transgenic rat models of ALS, which harbor the hSOD1 gene containing the H46R (His-46 → Arg) or G93A mutation were generated (Nagai et al., 2001). The larger size of these rat models makes certain experiments easier, such as biochemical analyses that require large amounts of sample, intrathecal administration

Contract grant sponsor: Core Research for Evolutional Science and Technology (CREST), Japan Science and Technology Agency (JST); Contract grant sponsor: Japanese Ministry of Health, Labour and Welfare; Contract grant sponsor: Japanese Ministry of Education, Culture, Sports, Science and Technology.

*Correspondence to: Hideyuki Okano, Department of Physiology, School of Medicine, Keio University, 35 Shinanomachi, Shinjuku-ku, Tokyo, 160-8582, Japan. E-mail: hidokano@sc.itc.keio.ac.jp

Received 22 August 2005; Revised 29 September 2005; Accepted 30 September 2005

Published online 7 December 2005 in Wiley InterScience (www.interscience.wiley.com). DOI: 10.1002/jnr.20708

of drugs, and, especially, therapeutic trials, including the transplantation of neural stem cells into the spinal cord. The hSOD1 (G93A) transgenic rats typically present weakness in one hindlimb first. Later, weakness progresses to the other hindlimb and to the forelimbs. Finally, the rats usually become unable to eat or drink, and eventually die. Only subjective and ambiguous analyses were made with regard to the clinical progression of this ALS animal model and objective criteria for evaluating the efficacy of these new treatments have not been determined. For these reasons, we assessed the disease progression quantitatively using five different measures (body weight, inclined plane test, cage activity, SCANET, and righting reflex) and established an easy, noninvasive, and objective evaluation system that is sensitive to small but important abnormalities in the hSOD1 (G93A) transgenic rats. In addition, we created a novel scale, the Motor score, to assess disease progression in the transgenic rats without using special apparatuses. We also examined the validity of these measures as assessment tools for the pathology by investigating the number of spinal motor neurons remaining at the disease stages defined by each measure.

MATERIALS AND METHODS

Transgenic Rats

All animal experiments were conducted according to the Guidelines for the Care and Use of Laboratory Animals of Keio University School of Medicine. We used hSOD1 (G93A) transgenic male rats (Nagai et al., 2001) from our colony and their age- and gender-matched wild-type littermates as controls. Rats were housed in a specific pathogen-free animal facility at a room temperature of 23 ± 1°C under a 12-hr light-dark cycle (light on at 08:00). Food (solid feed CE-2, 30kGy; CLEA Japan, Inc.) and water were available ad lib. Transgenic rats were bred and maintained as hemizygotes by mating transgenic males with wild-type females. Transgenic progeny were identified by detecting the exogenous hSOD1 transgene, by amplification of pup tail DNA extracted at 20 days of age by polymerase chain reaction (PCR). The primers and cycling conditions were described previously (Nagai et al., 2001).

Exploration of Assessment Tools to Measure Disease Progression in the hSOD1 (G93A) Transgenic Rats

We evaluated the usefulness of four different measures to assess disease progression in the transgenic rats. All tests were carried out between 12:00–16:00 and in a double-blind fashion.

Body weight. Animals ($n = 9$ for each genotype) were weighed weekly after 30 days of age with an electronic scale. To avoid overlooking the beginning of weight loss, the animals were weighed every second or third day after 90 days of age, the age at which motor neurons are reported to be lost in the lumbar spinal cord (Nagai et al., 2001).

Inclined plane. This test was initially established mainly to assess the total strength of the forelimbs and hindlimbs in a model of spinal cord injury (Rivlin and Tator, 1977). Briefly, rats were placed laterally against the long axis of the inclined plane, and the maximum angle at which they could maintain their position on the plane for 5 sec was measured. To assess the strength of both sides of limbs equally, animals were placed on the inclined plane with the right side of the body to the downhill side of the incline, and then with the left side of the body facing downhill. For each rat, the test was carried out three times for each side, and the mean value of the angles obtained for the right side was compared to that obtained for the left. The lower mean value was recorded as the angle for that rat. Animals ($n = 9$ for each genotype) were tested weekly after 70 days of age and every second to third day after 100 days of age.

Cage activity. Animals ($n = 8$ for each genotype) were housed individually and monitored every day for all 24 hr (except for the days the cages were changed) after they were 70 days old. Spontaneous locomotor activity in the home cage (345 × 403 × 177 mm) was recorded by an activity-monitoring system (NS-AS01; Neuroscience, Inc., Tokyo, Japan) as described previously (Ohki-Hamazaki et al., 1999). The sensor detects the movement of animals using the released infrared radiation associated with their body temperature. The data were analyzed by the DAS-008 software (Neuroscience, Inc., Tokyo, Japan). To eliminate data variability owing to differences in the baseline movement of each rat, the baseline value was calculated as the mean of movement from 70–90 days of age, during which all rats were considered to move normally. We analyzed the data at each time point as the percentage of the baseline value in defining disease onset with this test.

SCANET. For short-term activity, 10 min of spontaneous activity was measured with the automated motion analysis system SCANET MV-10 (Toyo Sangyo Co., Ltd., Toyama, Japan) (Mikami et al., 2002). Animals ($n = 4$ for each genotype) were tested weekly after 30 days of age and every second or third day after 100 days of age. Each rat was individually placed in the SCANET cage for 10 min. Three parameters were measured: small horizontal movements of 12 mm or more (Move 1; M1), large horizontal movements of 60 mm or more (Move 2; M2), and the frequency of vertical movements caused by rearing (RG). To distinguish RG movements from incomplete standing actions, the upper sensor frame was adjusted to 13 cm above the lower sensor frame.

Righting reflex. All affected animals were tested for the ability to right themselves within 30 sec of being turned on either side (righting reflex) (Gale et al., 1985). Failure was seen when animals reached the end-stage of disease (Howland et al., 2002), and was regarded as a generalized loss of motor activity. We used this time point, which we call "end-stage," as "death" rather than the actual death of the animal, to exclude the influence of poor food intake and respiratory muscle paralysis on the survival period. All end-stage animals were sacrificed after being deeply anesthetized.

All statistical analyses were carried out with the two-tailed unpaired Student's t-test. A P-value of <0.05 was considered statistically significant.

Motor Score

To establish our own scoring system for motor function, which could be uniformly applicable to any disease phenotype of this rat model, we examined the common clinical findings

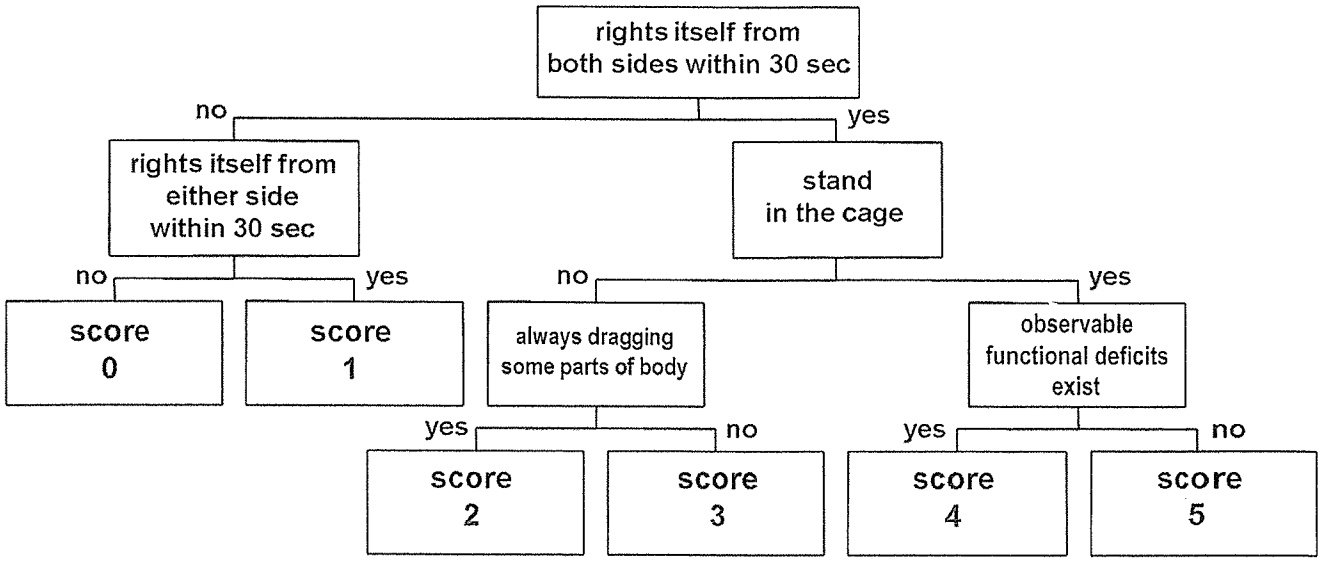

Fig. 1. Chart of Motor score assessment. The degree of motor dysfunction can be assessed by the Motor score as shown in this chart. This scoring system is meant to be used after disease onset, which can be prospectively diagnosed by the inclined plane test (muscle weakness onset). A score of 4 means the same condition as seen for subjective onset (SO). Rats with a score of 5 seem almost as normal as wild-type rats. The detailed testing procedure for the Motor score is described in the text.

of the transgenic rats in detail and assessed their motor functions ($n = 20$). We focused on the following tests: the righting reflex, the ability to stand in the cage, the extent of dragging their bodies when moving, and the existence of observable functional deficits. We evaluated these items sequentially along with the disease progression and classified the rats into six groups by giving them scores between 0 and 5. The scoring chart (Motor score) is shown in Figure 1.

When disease onset in the rats was diagnosed by their scoring $<70°$ on the inclined plane test (muscle weakness onset), the affected rats were tested for righting reflex. If they were unable to right themselves from either side, they were given a score of 0. If they could right themselves from only one side but not the other, they were given a score of 1.

Rats that could right themselves from both sides were examined for the ability to stand in the cage as follows: Rats were observed in the home cage for 1 min to see if they would stand spontaneously (Step 1). When they moved little in the home cage or showed no tendency to stand during Step 1, they were stimulated by being transferred to another cage (Step 2), and then by being returned to their home cage again (Step 3); the transfers were done to activate exploration motivation. During Step 3, the rats were further stimulated by lightly knocking the cage to intensify the motivation to explore. Each step was carried out for 1 min and the test was stopped when the rat stood once. Rats were judged as "unable to stand" if they did not stand, even after all three steps.

Rats that did not stand were subjected to the next test in the open field, where the extent to which they dragged their bodies when moving was assessed. Those who always dragged and could not lift some parts of their bodies except for scrotums and tails at any time were given a score of 2. If they could lift their dragging parts off the ground for even a moment, they were given a score of 3. The phenotype of dragging the forelimbs was different from that of dragging the hindlimbs. As disease progressed, "forelimb-type" rats first began to touch the tips of their noses on the ground, and then began to drag their head and upper trunk as they moved backward with their hindlimbs. "Hindlimb-type" rats dragged their lower trunk and moved forward with their forelimbs.

Finally, rats that had no abnormality in the above-mentioned assessments were examined in detail to see whether they had any observable functional deficits such as paralysis of the limbs or symptoms of general muscle weakness (e.g., walking with a limp, sluggish movement) in the open field. This condition could be judged subjectively and was defined as subjective onset. Rats with any of these symptoms were given a score of 4; otherwise they were given a score of 5.

Because the scores were based on subjective judgment, they might vary depending on the examiner. To examine inter-rater variability, three transgenic rats of different clinical types were examined according to the method described above, recorded on video tape, and subsequently scored by five observers from different backgrounds (Table I). The scores classified by the five observers were statistically analyzed for inter-rater agreement using Cohen's κ statistics (Table II). Kappa values can range from 0 (no agreement) to 1.00 (perfect agreement), and can be interpreted as poor (<0.00), slight (0.00–0.20), fair (0.21–0.40), moderate (0.41–0.60), substantial (0.61–0.80), and almost perfect (0.81–1.00) (Landis and Koch, 1977). The scores for the three transgenic rats were, on the whole, quite consistent among the five observers, suggesting that the Motor score can be used as an objective method for assessing disease progression.

TABLE I. Motor Score of Transgenic Rats Assessed by Five Different Observers

Transgenic rat	Observer	Days after onset (days) 0	1	2	3	4	5	6	7	8
#1407 Eventual hindlimb type										
	A	5	4	4		2	2	1	0	
	B	4	4	4		2	2	1	0	
	C	4	4	4		2	2	1	0	
	D	4	4	4		2	2	1	0	
	E	4	4	4		2	2	1	0	
	Mean	4.2	4	4		2	2	1	0	
#1470 Pure hindlimb type										
	A	5		4	4	2	2	2	2	0
	B	5		4	3	3	2	2	2	0
	C	5		4	3	2	2	2	2	0
	D	4		4	4	2	2	2	2	0
	E	4		4	3	2	2	2	2	0
	Mean	4.6		4	3.4	2.2	2	2	2	0
#1449 Pure forelimb type										
	A	4	3	3	3		2	1	1	0
	B	4	3	3	3		2	1	1	0
	C	3	3	3	3		2	1	1	0
	D	3	3	3	3		2	1	1	0
	E	4	3	2	2		2	1	1	0
	Mean	3.6	3	2.8	2.8		2	1	1	0

TABLE II. The kappa Statistics for Inter-Rater Agreement of Motor Score

Observers	Transgenic rat (clinical type) #1407 Eventual hindlimb	#1470 Pure hindlimb	#1449 Pure forelimb
A vs. B	0.82	0.69	1.00
A vs. C	0.82	0.82	0.83
A vs. D	0.82	0.81	0.83
A vs. E	0.82	0.70	0.69
B vs. C	1.00	0.83	0.83
B vs. D	1.00	0.53	0.83
B vs. E	1.00	0.66	0.69
C vs. D	1.00	0.64	1.00
C vs. E	1.00	0.82	0.54
D vs. E	1.00	0.81	0.54

TABLE III. Clinical Types of hSOD1 (G93A) Transgenic Rats

Clinical type	Subtype	*n*	%
Forelimb	Pure	4	8.2
	Eventual	5	10.2
Hindlimb	Pure	19	38.7
	Eventual	17	34.7
General		4	8.2
Total		49	100

Real-Time RT-PCR and Western Blot Analysis

Tissue specimens were dissected from the cerebral cortices, cerebella, medullae, and spinal cords (cervical, thoracic, and lumbar spinal cords) of the deeply anesthetized rats, and divided into two portions for total RNA and total protein preparation. Total RNA was isolated and first strand cDNA was synthesized as described previously (Okada et al., 2004). The real time RT-PCR analysis was carried out using Mx3000P (Stratagene, La Jolla, CA) with SYBR Premix Ex Taq (Takara Bio, Inc., Otsu, Japan). The primers used for the analysis were human *SOD1* (5′-TTGGGCAATGTGACTGCTGAC-3′, 5′-AGCTAGCAGGATAACAGATGA-3′), rat *SOD1* (5′-ACTTCGAGCAGAAGGCAAGC-3′, 5′-ACATTGGCCACACCGTCCTTTC-3′), and *β-actin* (5′-CGTGGGCCGCCCTAGGCACCA-3′, 5′-TTGGCCTTAGGGTTCAGAGGGG-3′). The results are presented as ratios of mRNA expression normalized to an inner control gene, *β-actin*. Total protein was prepared in lysis buffer containing 10 mM Tris-HCl (pH 7.6), 50 mM NaCl, 30 mM sodium pyrophosphate, 50 mM sodium fluoride, 20 mM glycerophosphate, 1% Triton X-100, and a protease inhibitor mixture (Complete; Roche Applied Science, Mannheim, Germany). Western blot analysis was carried out by a method established previously. In brief, a 5 μg protein sample of an extract was run on 12% SDS-PAGE, transferred to nitrocellulose, and probed with anti-human SOD1 (1:1,000, mouse IgG, Novocastra Laboratories, Ltd., Benton Lane, UK), and anti-α-tubulin (1:2,000, mouse IgG, Sigma-Aldrich, Inc., Saint Louis, MO). Signals were detected with HRP-conjugated secondary antibodies (Jackson ImmunoResearch Laboratories, Inc., West Grove, PA) using an ECL kit (Amersham Bioscience UK limited, Little Chalfont, UK). Quantitative analysis was carried out with a Scion Image (Scion Corporation, Frederick, MD). The amounts of proteins loaded in each slot were normalized to those of α-tubulin.

Immunohistochemical Analysis

Rats were deeply anesthetized (ketamine 75 mg/kg, xylazine 10 mg/kg, i.p.) and transcardially perfused with 4% paraformaldehyde/PBS (0.1 M PBS, pH 7.4) for histological examination. Spinal cord tissues were dissected out and post-fixed overnight in the same solution. Each spinal cord was dissected into segments that included the C6, T5, and L3 levels, immersed in 15% sucrose/PBS followed by 30% sucrose/PBS at 4°C, and embedded in Tissue-Tek O.C.T. Compound (Sakura Finetechnical Co., Ltd., Tokyo, Japan). Embedded tissue was immediately frozen with liquid nitrogen and stored at −80°C. Serial transverse sections of each spinal segment were cut on a cryostat at a thickness of 14 μm. The sections were pre-treated with acetone for 5 min, rinsed with PBS three times and permeabilized with TBST (Tris-buffered saline with 1% Tween 20) for 15 min at room temperature. After being blocked in the TNB buffer (Perkin-Elmer Life Sciences, Inc., Boston, MA) for 1 hr at room temperature, the sections were incubated at 4°C overnight with an anti-choline acetyltransferase (ChAT) polyclonal antibody (AB144P, Goat IgG, 1:50; Chemicon International, Inc., Temecula, CA). After being washed with PBS three times, the sections were incubated for 2 hr at room temperature with a biotinylated secondary antibody (Jackson ImmunoResearch Laboratories, Inc.). Finally, the labeling was developed using the avidin-biotin-peroxidase complex procedure (Vectastain ABC kits; Vector Laboratories, Inc., Burlingame, CA) with 3,3-diaminobenzidine (DAB; Wako Pure Chemical Industries, Ltd., Osaka, Japan) as the chro-

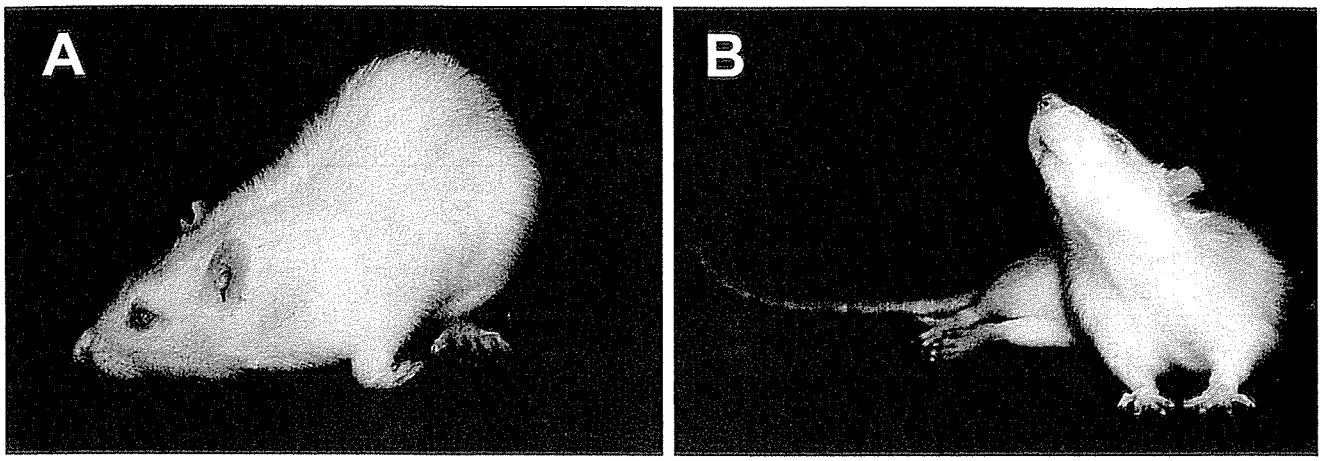

Fig. 2. Characteristic appearance of hSOD1 (G93A) transgenic rats. **A:** Forelimb type. The rat was unable to raise its head and was obligated to take a posture of raising the lumbar region, as indicated, because of the paralyzed forelimbs. **B:** Hindlimb type. The rat showed paraplegia, but was able to raise its head and upper trunk with its non-paralyzed forelimbs.

mogen. Immunohistochemical images were examined with a Zeiss-AxioCam microscope system.

Motor neurons bearing ChAT-immunoreactivity in laminae VII, VIII, and IX of the ventral horn were counted in every tenth section (5 sections total for each segment) for each of the C6, T5, and L3 segments. Only the neurons that showed labeling above background level and were larger than 20 μm in diameter were counted. The numbers of motor neurons in all segments (C6, T5, and L3) were summed for each animal to evaluate not only the local motor neuron loss, but the generalized loss of motor neurons throughout the spinal cord of each animal ($n = 3$ for each genotype at each time point). We next examined the correlation between the number of residual motor neurons and the results of the functional analyses described in this study. Statistical analysis was carried out with two-tailed unpaired Student's *t*-test. A *P*-value of <0.05 was considered statistically significant.

RESULTS

Clinical Types of hSOD1 (G93A) Transgenic Rats

Because we noticed variations in the disease phenotypes expressed by the G93A rats, we classified 49 rats into three clinical categories according to the location of initial paralysis. The clinical types were: the forelimb type, hindlimb type, and general type (Table III). Rats whose paralysis started in the forelimbs and progressed to the hindlimbs were defined as the "forelimb type." In contrast, rats whose paralysis started from the hindlimbs and progressed to the forelimbs were defined as the "hindlimb type." A typical appearance for the forelimb and hindlimb types is shown in Figure 2. Other rats, which showed simultaneous paralysis in the forelimbs and hindlimbs, were categorized as the "general type".

In addition, we classified the forelimb- and hindlimb-type rats into two subtypes, the pure and eventual types, based on the timing of the initial paralysis (Table III). Rats of the pure type showed paralysis that was limited to one or more of the four limbs as the initial observable deficit. Those of the eventual type initially showed symptoms of general muscle weakness (e.g., walking with a limp, sluggish movement), but without unequivocal limb paralysis. In the eventual type animals, paralysis of one of the limbs became apparent later. The ratio of each subtype is shown in Table III.

Evaluation of Disease Progression in the hSOD1 (G93A) Transgenic Rats

Although the transgenic rats varied in their clinical types, all four measures of disease progression (body weight, inclined plane test, cage activity, and SCANET) showed significant differences between the transgenic and wild-type rats (Fig. 3).

In contrast to the continuous weight gain in wild-type rats, the body weight in the affected rats ceased to increase and gradually decreased, with peak body weight attained around 110–120 days of age ($P < 0.05$, after 112 days of age) (Fig. 3A).

In the inclined plane test, initially both the transgenic and wild-type rats uniformly scored 75–80 degrees, after several training trials. However, the transgenic rats showed a significant decline in performance compared to their wild-type littermates from 120 days of age (Fig. 3B).

In the cage activity measurement, the movements of the wild-type rats remained stable, whereas those of the transgenic rats declined rapidly after 125 days of age (Fig. 3C).

In the SCANET test, even the wild-type rats showed decreased movements for all parameters (M1, M2, RG) in the late observation period, though they showed no abnormality in their motor functions. This might be because they had acclimated to the SCANET cage. The movement score of the transgenic rats was consistently worse than that of the wild-type rats after

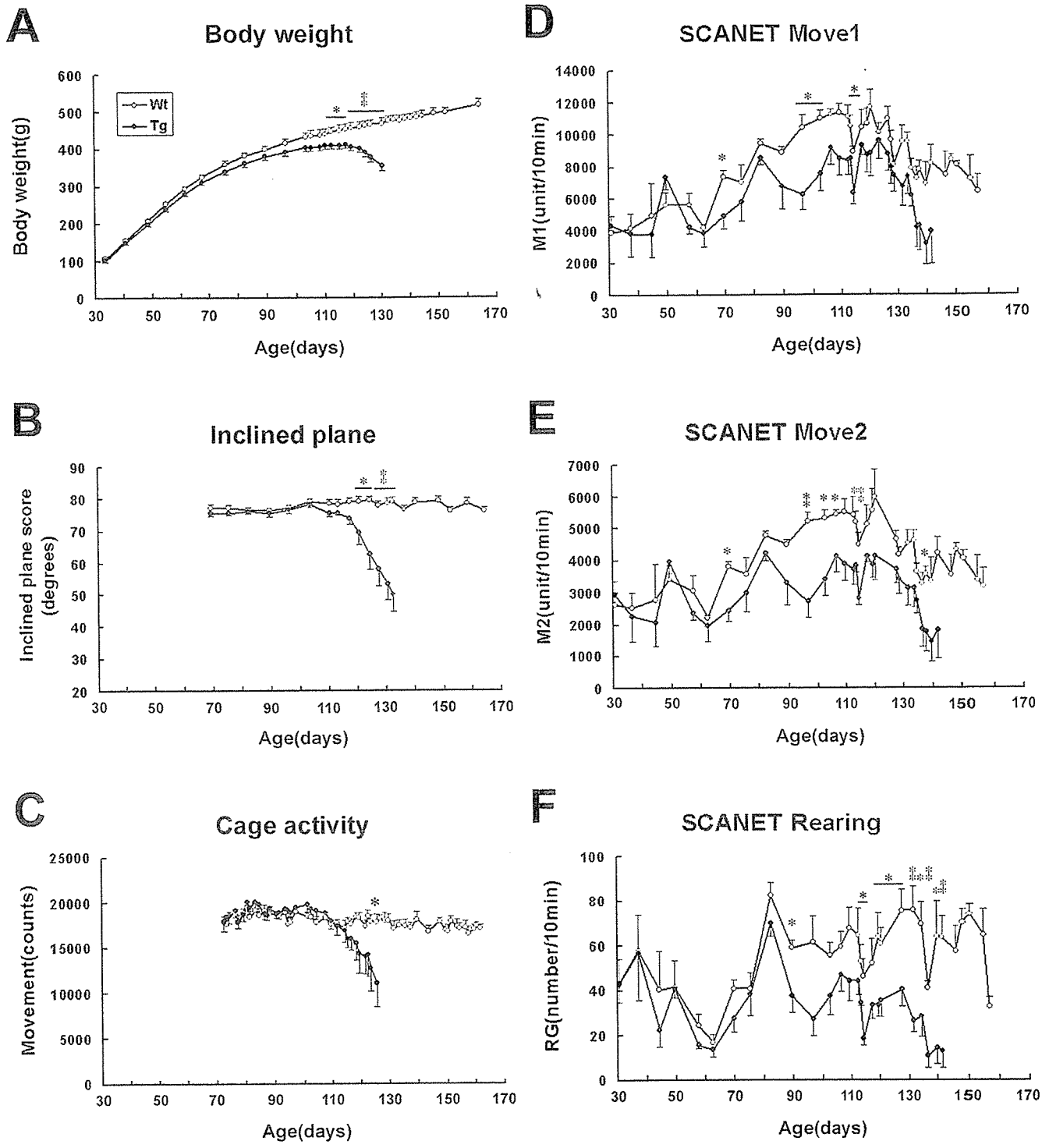

Fig. 3. Disease progression in hSOD1 (G93A) transgenic rats monitored by four effective measures. **A:** Body weight. The weight gain of the transgenic group stopped at around 110–120 days. The difference became statistically significant at 112 days of age ($n = 9$ for each genotype). **B:** Inclined plane. The wild-type group scored 75–80° throughout the period, whereas the score of the transgenic group declined. The difference became statistically significant at 120 days of age ($n = 9$ for each genotype). **C:** Cage activity. The movements of the wild-type group were stable, whereas the scores of the transgenic group declined. Significance was reached at 125 days of age ($n = 8$ for each genotype). **D–F:** SCANET. For all parameters (M1, M2, RG), the movement scores of the transgenic group became constantly worse than those of the wild-type group after 60 days of age. The differences between the groups increased markedly after 90 days of age. Significance was attained beginning at 67 days of age for M1 and M2, and at 87 days of age for RG ($n = 4$ for each genotype). The comparison between the wild-type and transgenic groups was stopped when the first of the transgenic rats reached the end-stage of the disease and was sacrificed. Mean ± SEM. $^{*}P < 0.05$. $^{**}P < 0.01$; two-tailed unpaired Student's *t*-test.